https://doi.org/10.5194/egusphere-2026-548
Preprint. Discussion started: 9 April 2026

Meso-NH-ISO v1.0: a water stable isotopes scheme in the non-hydrostatic mesoscale atmospheric model Meso-NH. Application to a 2D West African squall line

Christelle Barthe[1], Françoise Vimeux[2,3], Camille Risi[4], and Sören François[3]

[1]Laboratoire d'Aérologie (LAERO), Université de Toulouse, CNRS, IRD, Toulouse, France
[2]HydroSciences Montpellier (HSM), Université Montpellier, CNRS, IMT, IRD, Montpellier, France
[3]Laboratoire des Sciences du Climat et de l'Environnement (LSCE), CEA, CNRS, UVSQ, Université Paris-Saclay, Gif-sur-Yvette, France
[4]Laboratoire de Météorologie Dynamique (LMD), CNRS, ENS, X, UPMC, Paris, France

Correspondence: Christelle Barthe (christelle.barthe@cnrs.fr)

Abstract. Better understanding how convective processes impact the isotopic composition of atmospheric water has implications for understanding present-day phenomena such as squall lines or tropical cyclones, and for reconstructions of past rainfall extreme events. With this motivation, we implemented water stable isotopes in the non-hydrostatic mesoscale atmospheric model Meso-NH. Water stable isotopes are implemented in the advection of water phases and in the microphysical scheme. The implementation is validated on a test case of a 2D simulation of a tropical squall line observed in June 1981 during the COPT81 field campaign in the Sahel region. The isotopic version of Meso-NH (Meso-NH-ISO) captures the expected evolution of the isotopic composition of both precipitation and water vapor along the squall line. This work opens the door to future isotopic studies using realistic cases of mesoscale convective systems (squall lines, tropical cyclones).

Keywords. Cloud Resolving Model, Meso-NH, Water stable isotopes, Squall line

1 Introduction

The isotopic composition of water vapor and precipitation (δD and δ^{18}O) is a useful tool to better understand convective processes in the present-day water cycle, such as the contribution of rainfall evaporation to the moistening of the lower troposphere (Worden et al., 2007) or the contribution of convective detrainment and sublimation of ice crystals to the moistening of the upper troposphere and lower stratosphere (Moyer et al., 1996; Webster and Heymsfield, 2003; Hanisco et al., 2007).

The isotopic composition of precipitation recorded in climate archives has also significantly contributed to the reconstruction of past changes in precipitation in tropical regions (Wang et al., 2001; Cruz et al., 2009). This is based on the observation that precipitation is more depleted when precipitation rate is larger, called the amount effect (Dansgaard, 1964). Convective processes, such as convective downdraft, mesoscale descent, rain evaporation below cloud, and rain melt under stratiform clouds, contribute to the amount effect (Worden et al., 2007; Risi et al., 2008a; Kurita, 2013; Risi et al., 2021). Since these processes are expected to vary with the organization and characteristics of tropical convection, the water isotopic composition also depends on the proportion of stratiform versus convective rain (Aggarwal et al., 2016), on the mesoscale organization of

https://doi.org/10.5194/egusphere-2026-548
Preprint. Discussion started: 9 April 2026

convection (Lawrence et al., 2004; Risi et al., 2008b; Chakraborty et al., 2016; Vimeux et al., 2024) or on the convective depth (Moore et al., 2014; Torri et al., 2017; Lacour et al., 2017).

All these applications of water stable isotope observations require a better understanding of how convective processes impact the isotopic composition of water vapor and precipitation. So far, modeling studies have relied on models with parameterized convection (Lee et al., 2007; Bony et al., 2008), but these models are limited by the shortcomings and uncertainties associated with the parameterization of convection (Randall et al., 2003; Webb et al., 2015). To explicitly resolve convective motions, we need models that resolve the non-hydrostatic equations of motion at a resolution of the order of the kilometer or finer, such as cloud-resolving models or large-eddy simulation models. Several such models have been implemented with water stable isotopes in the past few years: DHARMA (Smith et al., 2006), SAM-ISO (Blossey et al., 2010), WRF-ISO (Moore et al., 2016), COSMO-ISO (Pfahl et al., 2012), and NICAM-WISO (Tanoue et al., 2023).

Here, we implemented water stable isotopes in the non-hydrostatic atmospheric model Meso-NH (Lac et al., 2018). This model is flexible enough to be used for idealized simulations, realistic case studies or global simulations, and can deal with scales ranging from synoptic to large eddy scales. In the past few years, it has taken part in various model intercomparison projects, such as RCEMIP (Wing et al., 2018) or DYAMOND (Stevens et al., 2019). Its physical package can also be shared with the LMDZ general circulation model (Hourdin et al., 2020) and can be used in the non-hydrostatic version of the icosahedral DYNAMICO model (Dubos et al., 2015). Our ultimate goal is to simulate realistic case studies with various mesoscale convective systems, including tropical cyclones and squall lines. In the meanwhile, a first step is to implement water stable isotopes in Meso-NH. The goal of this article is to describe this implementation, and to validate it on a simple case. The Meso-NH model and its one-moment microphysical scheme are shortly described in the first section. The second section is dedicated to the description of the newly implemented water isotope scheme in Meso-NH. In a thirst section, first results from a 2D simulation of a Sahelian squall line observed during the COPT81 field campaign are presented.

2 The Meso-NH model

The water stable isotopes scheme described in Sec. 3 is implemented in version 5-5-0 of the Meso-NH model, and is coupled to the one-moment bulk microphysics scheme (ICE3, Pinty and Jabouille, 1998).

2.1 Short overview of Meso-NH

Meso-NH is a non-hydrostatic mesoscale atmospheric model (Lac et al., 2018). It enables simulating atmospheric phenomena from the small-scale (down to a few meters) to the synoptic-scale (up to several tens of kilometers). A large set of physical parameterizations are available for convection (Bechtold et al., 2001; Pergaud et al., 2009), cloud microphysics (Pinty and Jabouille, 1998; Cohard and Pinty, 2000; Vié et al., 2016; Taufour et al., 2024), turbulence (Cuxart et al., 2000), gaseous chemistry (Tulet et al., 2003; Leriche et al., 2013), aerosols (Tulet et al., 2005, 2006), and cloud electricity including lightning flash production (Barthe et al., 2012). Two radiation schemes are available in Meso-NH, both originating from ECMWF (Morcrette, 1991; Mlawer et al., 1997) ; recently, the ecRad scheme (Hogan and Bozzo, 2018) has also become available.

https://doi.org/10.5194/egusphere-2026-548
Preprint. Discussion started: 9 April 2026

Meso-NH can be coupled with the surface modeling platform SurfEx (Masson et al., 2013) that accounts for natural land surface, urbanized areas, lakes, and oceans. Thus, Meso-NH offers a perfect setting for any simulation of physico-chemical processes in the atmosphere.

2.2 The ICE3 microphysics scheme

ICE3 is a bulk mixed-phase one-moment microphysics scheme (Caniaux et al., 1994; Pinty and Jabouille, 1998) that predicts the mass mixing ratio r of six water species (water vapor, cloud water, raindrops, primary ice crystals, snow aggregates, and graupel). For any species, the mixing ratio is the mass of the species divided by the reference mass of dry air ρ_a.

For cloud droplets, the total number concentrations (N_c) is fixed at 300×10^6 m^{-3} over land and 100×10^6 m^{-3} over oceans. For pristine ice, the total number concentration N_i is diagnosed based on the Meyers et al. (1992) parameterization of heterogeneous nucleation. The concentration of the precipitating particles (raindrops, snow/aggregates and graupel) is parameterized according to Caniaux et al. (1994), with the total number concentration given by $N = C\lambda^x$. C and x are empirical constants deduced from observations (see Table 1). λ is the slope parameter of the particle size distribution. In ICE3, the particle size distribution is assumed to follow a generalized Gamma distribution:

$$n(D) = Ng(D) = N\frac{\alpha}{\Gamma(\nu)}(\lambda D)^{\alpha\nu} D^{-1} e^{-(\lambda D)^{\alpha}} \tag{1}$$

where D is the diameter of the particle, $g(D)$ the normalized generalized Gamma distribution and $\Gamma()$ the Gamma function. α and ν are free shape parameters; their values are given in Table 1. The pth moment of the law writes:

$$M(p) = \int_0^{\infty} D^p g(D)\, dD = \frac{1}{\lambda^p}\frac{\Gamma(\nu + p/\alpha)}{\Gamma(\nu)} \tag{2}$$

It is also assumed that the mass (m) and terminal fall speed (v) of hydrometeors are related to the particle diameter D following power laws:

$$m(D) = aD^b \tag{3}$$

and

$$v(D) = cD^d \left(\frac{\rho_0}{\rho_a}\right)^{0.4} \tag{4}$$

where a, b, c and d are constants given in Table 1. ρ_0 is the reference air density at the surface. Then the mixing ratio is defined by:

$$r = \int_0^{+\infty} m(D)n(D)dD = aNM(b) \tag{5}$$

while the slope parameter of the particle size distribution writes:

$$\lambda = \left(\frac{\rho_a r \Gamma(\nu)}{aN\Gamma(\nu + b/\alpha)}\right)^{-1/b} \tag{6}$$

https://doi.org/10.5194/egusphere-2026-548
Preprint. Discussion started: 9 April 2026

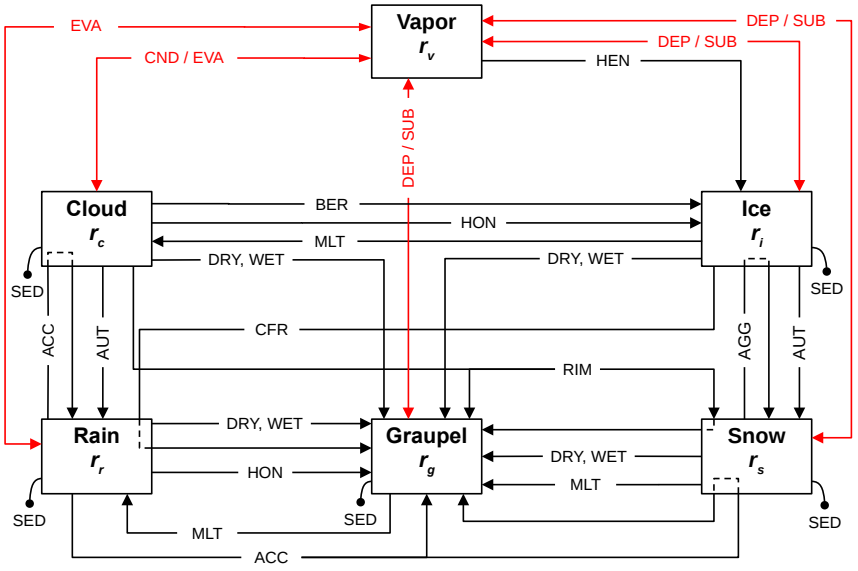

Figure 1. Diagram of the microphysical processes of ICE3. Red arrows show processes involving isotopic fractionation.

Each type of hydrometeor has one or more initiation and growth processes as shown in Fig. 1. Warm-phase processes are based on the Kessler (1969) scheme. Raindrops are formed by autoconversion of cloud droplets (AUT), grow through accretion of cloud droplets (ACC), and can evaporate (EVA). Pristine ice crystals are initiated through heterogeneous nucleation (HEN) or by homogeneous nucleation (HON) when the temperature is below -35°C. These ice crystals grow by deposition (DEP) and through the Bergeron-Findeisen process (BER). Snow/aggregates are formed by autoconversion of pristine ice crystals (AUT), then grow by aggregation of ice crystals (AGG) and by light riming due to collection of cloud droplets (RIM) or to accretion of raindrops (ACC). Then graupel are formed by heavy riming of snow (RIM and ACC) or by contact freezing of ice crystals on raindrops (CFR). They further grow by dry and wet growth mode (DRY, WET). Snow/aggregates and graupel can grow or decay by water vapor deposition (DEP) or sublimation (SUB). When the temperature drops below 0°C, ice crystals are immediately transformed into cloud droplets (MLT). Snow/aggregates are converted progressively into graupel particles that melt while falling. The fast vapor exchanges with cloud droplets (CND/EVA) and pristine ice crystals (DEP/SUB) are treated using an implicit adjustment scheme.

The time-step dependency in the original ICE3 scheme is suppressed according to Riette (2020).

https://doi.org/10.5194/egusphere-2026-548
Preprint. Discussion started: 9 April 2026

3 Water stable isotopes implementation in Meso-NH

3.1 Water stable isotope variables

The introduction of water isotopologues into Meso-NH was achieved using a similar approach to previous studies in the development of isotopic models (e.g. Blossey et al., 2010). Analogously, the original water prognostic variables in the model are taken to represent the most common standard light water, $H_2^{16}O$. To integrate heavy isotopes in Meso-NH, prognostic variables and equations describing the water cycle of each isotopologue are introduced into the model. As for light water, the mass mixing ratio of each heavy water isotopologue (r^{iso}) for each water species is a prognostic variable of the model. In practice, each water variable is duplicated twice, for heavy molecules $HD^{16}O$ and $H_2^{18}O$. Therefore 12 additional variables are implemented in the model. These additional variables are subject to the same physical processes as the light water variables, and evolve according to:

$$\frac{\partial}{\partial t}(\rho_a r^{\mathrm{iso}}) + (\rho_a r^{\mathrm{iso}}\mathbf{U}) = \rho_a S^{\mathrm{iso}} \tag{7}$$

where $\mathbf{U}$ is the 3D air velocity. The source term S^{iso} includes the turbulent diffusion, the sedimentation by gravity, the microphysical evolution of the particles, and their isotopic fractionation.

The mass exchange of heavy isotopes during microphysical processes not involving isotopic fractionation, is proportional to their relative mass mixing ratio in the source species. Thus, for each microphysical process without isotopic fractionation, the mass transfer rate for heavy water (Δr^{iso}) is proportional to the mass transfer rate calculated for standard water provided by the microphysics scheme (Δr). For example, during the accretion of cloud droplets by snow (ACC), the mass mixing ratio transfer rate for $HD^{16}O$ and $H_2^{18}O$ writes:

$$\Delta r^{\mathrm{iso}}\big|_{\mathrm{ACC}} = \Delta r|_{\mathrm{ACC}} \times \frac{r^{\mathrm{iso}}}{r} \tag{8}$$

In the case of microphysical processes involving phase change, new equations are implemented in the model to deal with isotopic fractionation; they are described in Section 3.2.

During the post-processing of model outputs, several diagnostics are computed. The isotope ratio R is defined for each water species as r^{iso}/r. Then, the isotopic composition (δ) is quantified by comparing the isotope ratio R for a water species to the isotope ratio in a standard (R_{VSMOW} where VSMOW stands for Vienna Standard Mean Ocean Water):

$$\delta = \left[\frac{R}{R_{\mathrm{VSMOW}}} - 1\right] \times 1000 \tag{9}$$

$\delta^{18}O$ and δD quantify the relative proportion of $H_2^{18}O$ and HDO, respectively. Finally, the deuterium excess (d-excess), an indicator of the kinetic effects associated with phase changes (Dansgaard, 1964), is computed for each hydrometeor:

$$\mathrm{d-excess} = \delta\mathrm{D} - 8 \times \delta^{18}\mathrm{O} \tag{10}$$

https://doi.org/10.5194/egusphere-2026-548
Preprint. Discussion started: 9 April 2026

3.2 Isotopic fractionation

Isotopic fractionation occurs due to differences in mass and symmetry between the different water molecules. Molecular mass differences induce equilibrium fractionation. Due to a lower saturation vapor pressure for heavy isotopes, the heavier molecules concentrate in the condensed phase. Additionally, kinetic fractionation is induced by diffusivity differences, with a lower diffusivity of heavy isotopes. Then, in order to provide a comprehensive understanding of the distribution of isotopes in water and of the related physical processes, it is necessary to take into account both equilibrium and kinetic fractionation processes that occur during water phase changes.

The following sections explain how isotope fractionation processes are incorporated into Meso-NH. Logic variables controlling the code segments of the model that account for isotopic fractionation can be enabled or disabled to simplify sensitivity analysis, as used by Arnault et al. (2021).

3.2.1 Condensation and evaporation of cloud water

In the ICE3 microphysics scheme, as in most one-moment bulk microphysics scheme, the parameterization of the condensation/evaporation processes consists of a saturation adjustment aimed at restoring the thermodynamic equilibrium between water vapor and cloud droplets. Since the equilibration time for small droplets is normally of the order of seconds, an equilibrium approach may also be used for heavy isotopes (Blossey et al., 2010). Thus, the isotopic fractionation that occurs during droplet condensation within the cloud is considered to be at equilibrium (Bony et al., 2008; Blossey et al., 2010; Arnault et al., 2021), and the differences in molecular diffusivity between the molecules are not taken into account.

At equilibrium:

$$R_c = \alpha_{l/v} \times R_w \tag{11}$$

where R_c and R_w are the isotopic composition of cloud droplets and water vapor, respectively, and $\alpha_{l/v}$ is the isotopic equilibrium fractionation factor over liquid. Then if the water variables are advanced by one model time step:

$$\frac{r_c^{\mathrm{iso}} + \Delta r^{\mathrm{iso}}\big|_{\mathrm{CND/EVA}}}{r_c + \Delta r|_{\mathrm{CND/EVA}}} = \alpha_{l/v} \times \frac{r_v^{\mathrm{iso}} - \Delta r^{\mathrm{iso}}\big|_{\mathrm{CND/EVA}}}{r_v - \Delta r|_{\mathrm{CND/EVA}}} \tag{12}$$

Given $B = \frac{r_c + \Delta r|_{\mathrm{CND/EVA}}}{r_v - \Delta r|_{\mathrm{CND/EVA}}}$, Eq. 12 leads to:

$$\Delta r^{\mathrm{iso}}\big|_{\mathrm{CND/EVA}} = \frac{\alpha_{l/v} r_v^{\mathrm{iso}} B - r_c^{\mathrm{iso}}}{1 + \alpha_{l/v} B} \tag{13}$$

Cloud droplets evaporation is also treated in Eq. 13 when $\Delta r|_{\mathrm{CND/EVA}}$ is negative; it is also assumed to be at equilibrium.

3.2.2 Rain evaporation

For raindrops, due to their larger size, the isotopic equilibrium assumption is not valid, and the mass transfer between the drop and the surrounding vapor must be modeled explicitly. In Meso-NH, the evaporation rate of a raindrop is derived following

https://doi.org/10.5194/egusphere-2026-548
Preprint. Discussion started: 9 April 2026

Pruppacher and Klett (1997) and Seinfeld and Pandis (2016), and the rate of change of a raindrop mass (m_r) finally writes

$$\left.\frac{dm_r}{dt}\right|_{\text{EVA}} = 4\pi \mathcal{C}_1 D f S_l A_w^{-1} \tag{14}$$

where D is the raindrop diameter, f the mean ventilation coefficient, $\mathcal{C}_1$ the parameter of the capacitance-diameter relationship (see values in Table 1), and S_l the supersaturation over liquid water. A_w is a thermodynamic function that writes

$$A_w = \frac{\mathcal{R}_v T}{e_{\text{sw}}(T) D_v} + \frac{L_v^2}{k_a \mathcal{R}_v T^2} \tag{15}$$

with $\mathcal{R}_v$ the specific gas constant for water vapor, $e_{\text{sw}}(T)$ the saturation vapor pressure at the ambient temperature T, L_v the latent heat of vaporization, and k_a the heat conductivity of air. $\mathcal{D}_v$ is the molecular diffusivity of light water vapor in air. As established by Hall and Pruppacher (1976) for temperatures between -80 and 40°C, it follows:

$$\mathcal{D}_v = 0.211 \left(\frac{T}{T_0}\right)^{1.94} \left(\frac{p_0}{p}\right) \tag{16}$$

with p the pressure, T_0 = 273.15 K and p_0 = 1013.25 mb.

The mean ventilation coefficient f is parameterized following Pruppacher and Klett (1997):

$$f = f_0 + f_1 \chi + f_2 \chi^2 \tag{17}$$

where $\chi = N_{\text{Sc,v}}^{1/3} N_{\text{Re}}^{1/2}$, and f_0, f_1 and f_2 are ventilation coefficients which values follow Pruppacher and Klett (1997) and are given in Table 1. $N_{\text{Sc,v}}$ is the Schmidt number for water vapor; it is set to 0.63. N_{Re} is the Reynolds number of the flow around a particle of diameter D:

$$N_{\text{Re}} = \frac{v(D) D}{\nu(T)} = \frac{v(D) D \rho_a}{\eta(T)} \tag{18}$$

with $\nu(T)$ the kinematic viscosity of air, and $\eta(T)$ (Pa s) the dynamic viscosity of air which can be approximated by $\eta(T) = 1.718\ 10^5 + 0.0049\ 10^5 (T - T_0)$ (Pruppacher and Klett, 1997).

To get the mass mixing ratio rate of change for raindrops, Eq. 14 is integrated over the whole size distribution

$$\Delta r_r|_{\text{EVA}} = \frac{1}{\rho_a} 4\pi \mathcal{C}_1 S_l A_w^{-1} \int_0^\infty D(f_0 + f_1 \chi + f_2 \chi^2) n(D) dD \tag{19}$$

By replacing the Reynolds number with its expression in χ and substituting the expression for $v(D)$ from Eq. 4

$$\chi = N_{\text{Sc,v}}^{1/3} \times \left(\frac{\rho_0}{\rho_a}\right)^{0.2} \left(\frac{\rho_a c D^{d+1}}{\eta(T)}\right)^{1/2} \tag{20}$$

If $c' = N_{\text{Sc,v}}^{1/3} \times \left(\frac{\rho_0}{\rho_a}\right)^{0.2} \left(\frac{\rho_a c}{\eta(T)}\right)^{1/2}$, the expression of $\chi = c' D^{\frac{d+1}{2}}$ is introduced in Eq. 19. Using the definition of the pth moment of the size distribution law (Eq. 2), the variation in raindrop mixing ratio during evaporation is

$$\Delta r_r|_{\text{EVA}} = \frac{1}{\rho_a} 4\pi \mathcal{C}_1 S_l A_w^{-1} N \left[f_0 M(1) + f_1 c' M\left(\frac{d+3}{2}\right) + f_2 c' M(d+2) \right] \tag{21}$$

https://doi.org/10.5194/egusphere-2026-548
Preprint. Discussion started: 9 April 2026

Assuming $f_2 = 0$ for raindrops (Table 1) in Eq. 21, the mixing ratio transfer rate for evaporating raindrops is

$$\Delta r_r|_{\text{EVA}} = \frac{1}{\rho_a} 4\pi \mathcal{C}_1 S_l A_w^{-1} N \left[f_0 M(1) + f_1 c' M \left(\frac{d+3}{2} \right) \right] \tag{22}$$

For $H_2^{18}O$ and $HD^{16}O$ isotopologues, Eq. 13.53 in Pruppacher and Klett (1997) writes

$$\left. \frac{dm_r^{\text{iso}}}{dt} \right|_{\text{EVA}} = 4\pi \mathcal{C}_1 D \mathcal{D}_v^{\text{iso}} f^{\text{iso}} \left(\rho_w^{\text{iso}} - \rho_{w,D}^{\text{iso}} \right) \tag{23}$$

with m^{iso} the mass of a raindrop of diameter D containing heavy isotopes, and ρ_w^{iso} and $\rho_{w,D}^{\text{iso eq}}$ the density of heavy water vapor for the environment and on the surface of the raindrop, respectively. The molecular diffusivity of the heavy molecules $\mathcal{D}_v^{\text{iso}}$ is deduced from the molecular diffusivity of standard water, $H_2^{16}O$, with the ratio of the diffusivity coefficients $\mathcal{D}_v^{iso}/\mathcal{D}_v$ obtained from the experiments of Merlivat (1978) for $H_2^{18}O$ and $HD^{16}O$. f^{iso} is the mean ventilation factor for heavy water: $f^{\text{iso}} = f_0 + f_1 \chi_{\text{iso}} + f_2 \chi_{\text{iso}}^2$ with $\chi_{iso} = (N_{\text{Sc,v}}^{\text{iso}})^{1/3} N_{\text{Re}}^{1/2}$. The same f_0, f_1 and f_2 parameters as for light water are used (Table 1). However, the Schmidt number is scaled with the specific molecular diffusivity of the heavy molecules: $\text{N}_{\text{Sc,v}}^{\text{iso}} = \text{N}_{\text{Sc,v}} \times \mathcal{D}_v / \mathcal{D}_v^{\text{iso}}$. Using the same reasoning as for light water to derive the variation in mass of an evaporating raindrop of heavy isotope water, the rate of change of a raindrop containing heavy isotopes is

$$\left. \frac{dm_r^{\text{iso}}}{dt} \right|_{\text{EVA}} = 4\pi \mathcal{C}_1 D \mathcal{D}_v^{\text{iso}} f^{\text{iso}} \frac{e_{\text{sw}}(T)}{\mathcal{R}_v T} \left[R_w (S_l + 1) - \frac{R_l}{\alpha_{l/v}} \left(1 + \frac{L_v^2}{\mathcal{R}_v k_a f^{\text{iso}} D T^2} \left. \frac{dm_r}{dt} \right|_{\text{EVA}} \right) \right] \tag{24}$$

with R_w and R_l are the isotopic ratio in water vapor and liquid condensate, respectively, and $\alpha_{l/v} = R_l / R_w$ the isotopic fractionation factor between liquid and vapor. This equation can thus be integrated over the raindrop size distribution to get the evolution of the raindrop mixing ratio for heavy isotope water

$$\Delta r_r^{iso}|_{\text{EVA}} = \frac{1}{\rho_a} 4\pi \mathcal{C}_1 \mathcal{D}_v^{\text{iso}} \frac{e_{\text{sw}}(T)}{\mathcal{R}_v T} N \left[\left(R_w (S_l + 1) - \frac{R_l}{\alpha_{l/v}} \right) \left(f_0 M(1) + f_1 c'^{\text{iso}} M \left(\frac{d+3}{2} \right) \right) + \frac{R_l}{\alpha_{l/v}} \frac{L_v^2}{\mathcal{R}_v k_a T^2} \rho_a \, \Delta r_r|_{\text{EVA}} \right] \tag{25}$$

with $c'^{\text{iso}} = (N_{\text{Sc,v}}^{\text{iso}})^{1/3} \times \left(\frac{\rho_0}{\rho_a} \right)^{0.2} \left(\frac{\rho_a c}{\eta(T)} \right)^{1/2}$

3.2.3 Diffusional growth of ice hydrometeors

For ice particles, an equation similar to the one for liquid particles (Eq. 14) is derived in the ICE3 scheme:

$$\left. \frac{dm}{dt} \right|_{\text{DEP}} = 4\pi \mathcal{C}_1 D S_i A_i^{-1} f \tag{26}$$

with S_i the supersaturation over ice, and A_i a thermodynamic function that writes

$$A_i = \frac{\mathcal{R}_v T}{e_{\text{si}}(T) D_v} + \frac{L_s^2}{k_a \mathcal{R}_v T^2} \tag{27}$$

https://doi.org/10.5194/egusphere-2026-548
Preprint. Discussion started: 9 April 2026

with L_s the latent heat of sublimation ($\mathrm{J\,kg^{-1}}$), $e_{\mathrm{si}}(T)$ the saturation vapor pressure over ice (Pa) at ambient temperature T.

In the case of heavy isotopes, the same approach as Blossey et al. (2010) in SAM-iso is followed. By analogy with the evaporation of rain, the rate of change of the mass of a precipitating ice particle can write:

$$\left.\frac{dm^{\mathrm{iso}}}{dt}\right|_{\mathrm{DEP}} = 4\pi\mathcal{C}_1 D\mathcal{D}_v^{\mathrm{iso}} f^{\mathrm{iso}} \frac{e_{si}(T)}{\mathcal{R}_v T}\left[R_w(S_i+1) - \frac{R_i}{\alpha_{i/v}}\left(1 + S_i A_i^{-1}\frac{L_s^2}{\mathcal{R}_v k_a T^2}\right)\right] \tag{28}$$

with R_i the isotopic ratio in ice, and $\alpha_{i/v}$ the equilibrium fractionation factor between ice and water vapor. Due to the low diffusivity of heavy isotopes, it is assumed that water vapor interact with a thin layer at the surface of ice particle during deposition. Then the ratio r^{iso}/r in the outer layer can be approximated by the ratio $(\Delta r^{\mathrm{iso}}|_{\mathrm{DEP}} / \Delta r|_{\mathrm{DEP}})$ at the surface of ice particle. Therefore, the isotopic ratio in ice also writes

$$R_i = \frac{\Delta r^{iso}|_{\mathrm{DEP}}}{\Delta r|_{\mathrm{DEP}}} \tag{29}$$

Using Eq. 26 in Eq. 28 to eliminate $\mathcal{C}_1$, one finally get

$$\Delta r|_{\mathrm{DEP}} = \alpha_{i/v}\alpha_K R_w\ \Delta r|_{\mathrm{DEP}} \tag{30}$$

where α_K is the kinetic fractionation coefficient defined by Jouzel and Merlivat (1984):

$$\alpha_K = \frac{(1+F)(S_i-1)}{\alpha_{i/v}\frac{f\mathcal{D}_v}{f^{\mathrm{iso}}\mathcal{D}_v^{\mathrm{iso}}}S_i + 1 + F(S_i-1)} \tag{31}$$

with $F = \frac{\mathcal{D}_v L_s^2 e_{si}(T)}{k_a \mathcal{R}_v^2 T^3}$.

Sublimation of ice, snow and graupel particles is assumed to occur without isotopic fractionation. As in previous studies (Bony et al., 2008; Blossey et al., 2010; Pfahl et al., 2012), it is assumed that the mass transfer rate for heavy water (Δr^{iso}) associated with sublimation is proportional to the mass transfer rate calculated for standard water and provided by the microphysics scheme ($\Delta r|_{\mathrm{SUB}}$) ratio equal to its mean ratio

$$\Delta r^{\mathrm{iso}}|_{\mathrm{SUB}} = \frac{r^{\mathrm{iso}}}{r} \times \Delta r|_{\mathrm{SUB}} \tag{32}$$

where r and r^{iso} are the mixing ratio of ice, snow or graupel for $H_2^{16}O$, and $H_2^{18}O$ or $HD^{16}O$, respectively.

4 Simulation of a 2D Sahelian squall line

4.1 The West African squall line on June 23-24, 1981 during COPT 81

We tested Meso-NH-ISO with a 2D simulation of a West African squall line that was fully observed (Roux et al., 1984; Chong et al., 1987; Chalon et al., 1988; Roux, 1988) and simulated with different 2D and 3D numerical experiments (Redelsperger and Lafore, 1988; Lafore and Moncrieff, 1989; Chang and Yoshizaki, 1993; Caniaux et al., 1994). This tropical squall line occurred during the night of 23 to 24 June 1981 during the COPT81 measurement campaign in the northern Ivory Coast

https://doi.org/10.5194/egusphere-2026-548
Preprint. Discussion started: 9 April 2026

(5°37'W, 9°25'N). This case was chosen because a previous simulation was done with a 2D version of Meso-NH (Caniaux et al., 1994) and successfully reproduced the major observed features. In short, the radar observations clearly identified an intense convective region, a well-developed stratiform part with a forward anvil cloud, and the transition zone in between (Chalon et al., 1988). Specifically, the squall line exhibited in its convective part a line of short-live convective cells that fastly propagated (around 50 $\mathrm{km\,h^{-1}}$) toward the south-east. In the stratiform region, a trailing anvil cloud developed above 6 km. Chalon et al. (1988) estimated that 80 % of precipitation occurred in the convective region, whereas the rest occurred in the stratiform region. They also roughly estimated substantial evaporation of rain droplets (around 40 %) in the stratiform region below the anvil cloud. A density current of cold air in the stratiform region induced a low-level frontward flow that initiated and maintained updrafts in convective region. We also chose to test Meso-NH-ISO with a squall line simulation due to the isotopic observations available in both water vapor and precipitation in the West African region during such events, and idealized simulations of such events in previous studies (Risi et al., 2008a, 2010, 2023; Tremoy et al., 2014)

4.2 Simulation set-up

The horizontal axis is composed of 320 grid-points with a horizontal grid spacing of 1.25 km. The vertical grid contains 46 levels up to an altitude of 22 km, with a grid spacing varying from 70 m on the ground to 700 m at the top of the domain.

The simulation is initialized following Caniaux et al. (1994). The atmosphere is initially homogeneous and the initial sounding for temperature and humidity comes from Redelsperger and Lafore (1988). The isotopic composition of water vapor is initialized following a Rayleigh distillation, assuming initial conditions at the surface of $\delta\mathrm{D}_v = -110\,‰$ and $\delta^{18}\mathrm{O}_v = -15\,‰$, leading to d-excess$_v$ = 10 ‰, consistent with initial conditions in Risi et al. (2010).

A cold pool is used to initiate convection: a 0.01 K cooling rate is applied for 10 min in a region 12 km long and 4 km height. Open boundary conditions are used in the x-direction, with periodic conditions. There are no lateral advection. A Galilean transformation of 13 $\mathrm{m\,s^{-1}}$ is applied all along the simulation to keep the convective system in the simulation domain. The simulation lasts 8 h which corresponds to the time needed by the squall line to reach and stay in a mature stage according to Caniaux et al. (1994).

The one-moment ICE3 microphysics scheme (Pinty and Jabouille, 1998) presented in Sec. 2.2 was used, along with the water stable isotope scheme. A 3D turbulence scheme (Cuxart et al., 2000) was also activated.

For the sake of simplicity, surface fluxes are deactivated. This is justified by the fact that over the 8 hours of simulations, the influence of surface fluxes is small, and there is no time to reach an equilibrium between surface fluxes and precipitation.

4.3 Steady-state

Figure 2 shows the evolution of precipitation rate and the isotopic composition of precipitation at the surface along the course of the simulation. The squall line builds and precipitation rate grows during the first 5 hours of the simulation. Then, precipitation rate reaches a plateau between 5 and 6 hours before declining. During the last 3 hours of the simulation, the isotopic composition of precipitation ($\delta^{18}\mathrm{O}_p$, $\delta\mathrm{D}_p$ and d-excess$_p$) settles into a quasi-steady state. Figure 3 shows the same for the

https://doi.org/10.5194/egusphere-2026-548
Preprint. Discussion started: 9 April 2026

near-surface water vapor. Although specific humidity reaches a steady state after 5 hours, the isotopic composition of water vapor ($\delta^{18}O_v$, δD_v) keeps depleting, suggesting that the simulation is not into steady-state for this phase.

We investigated to understand why the isotopic composition of rain reaches a quasi-steady state in contrast to the isotopic composition of water vapor. During the simulation, convective mixing dries out and depletes the boundary layer (below 1.5 km) and moist and enriches the free troposphere (Fig. S1a-b). These trends persist throughout the simulation, fading at the end of the simulation as convection weakens significantly after 6-7 hours. Specific humidity reaches a quasi-steady state at the end of the simulation because the drying effect of convective mixing is offset by the moistening effect of droplet evaporation (Fig. S1c). The isotopic composition of water vapor does not reach equilibrium at the end of the simulation because the depleted effect of convective mixing is reinforced by the depleted effect of droplet evaporation. The isotopic composition of the precipitation appears to reach equilibrium, but this is because two effects compensate each other: (1) the water vapor in the boundary layer, with which the rain equilibrates, is increasingly depleted, so it tends to deplete the rain; (2) the water vapor in the free troposphere, where the droplets form, is more enriched, so it tends to enrich the rain (Fig. S1d).

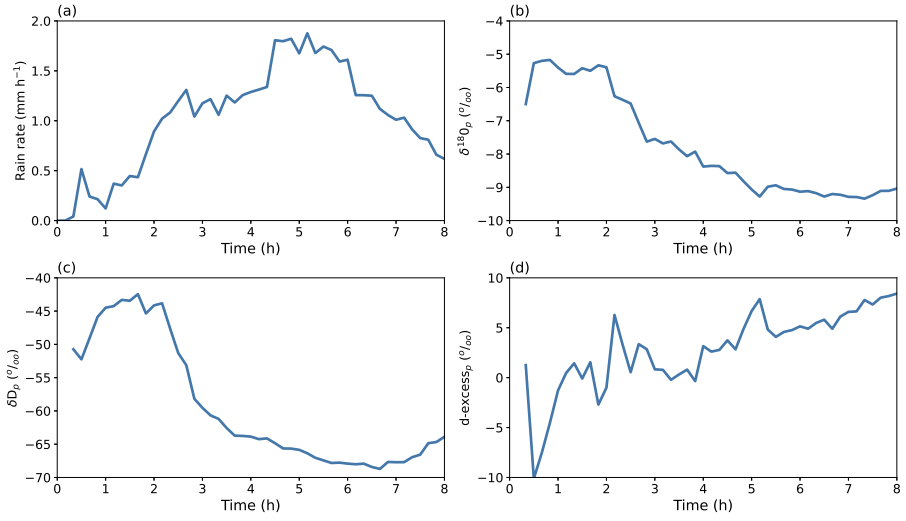

Figure 2. Temporal evolution of (a) the instantaneous surface rain rate ($\mathrm{mm\,h^{-1}}$), and the isotopic composition of the rain (‰): (b) $\delta^{18}O$, (c) δD and (d) d-excess. Variables are averaged over the whole domain every 10 min.

4.4 Structure and dynamics of the squall line

We describe here the structure and the dynamic of the squall line after 6 hours of simulation when rain rate is at its highest level and the squall line has reached a mature stage (as already observed in the simulation done by Caniaux et al. (1994)). Figure 4 shows the cross section of several parameters sensitive to squall line's structure and dynamic that are shown schematically on Fig. 5 for a better understanding of the description of Fig. 4.

https://doi.org/10.5194/egusphere-2026-548
Preprint. Discussion started: 9 April 2026

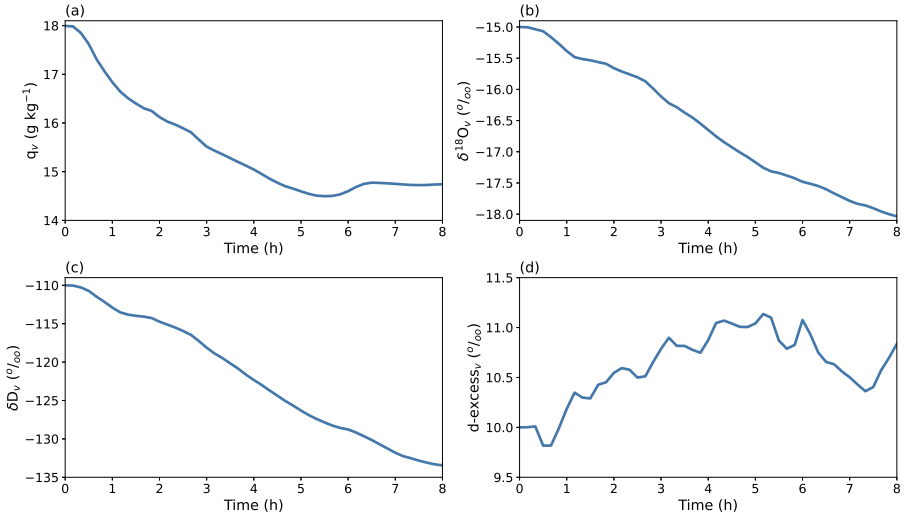

Figure 3. Temporal evolution of (a) the near-surface water vapor mixing ratio (g kg^{-1}), and the isotopic composition of water vapor (‰): (b) δ^{18}O, (c) δD and (d) d-excess. Variables are averaged over the whole domain every 10 min.

Figures 4a and 4b show the cross section of the condensed (liquid and ice) water and rain contents respectively along the x-direction. Strong values of condensed water content correspond to strong updrafts. In both snapshots, we can see that there is a series of several updrafts from about 135 to 165 km, about 10 km apart from each other, corresponding to various convective cells at different stages, from the shallowest near the front of the squall line (at around 135 km) to the deepest at the rear (at around 165 km), consistent with previous studies (Gamache and Houze, 1981; Houze, 1977; Lafore et al., 1988).

Figures 4c and 4e show the cross section of the relative humidity and the moist static energy respectively. The high values of relative humidity near or at saturation correspond to the cloud, while lower values correspond to the environment or to subsiding air. The high values of moist static energy correspond to ascending air from the boundary layer to higher altitude, whereas lower values correspond to mid-tropospheric environment or subsiding air. The two snapshot exhibit expected features for well-developed squall lines. We can clearly see the convective region composed of several convective updrafts transporting air from the boundary layer to higher levels from about 135 to 165 km as mentioned above (high relative humidity and moist static energy). We also clearly detect lower relative humidity and moist static energy within downdrafts. The stratiform region is clearly developed. It corresponds to the cloudy area that extends behind the convective zone above around 4 km height from about 195 to 260 km. Below the stratiform region, the cold pool is identified by the dry air with low moist static energy (Fig. 4c and 4e). It extends frontwards towards the front of the line, around 130 km. Between convective and stratiform zones, the transition region is identified in the simulation by patches of dry subsiding air between around 165 an 195 km and below 4 km height (Fig. 4c).

https://doi.org/10.5194/egusphere-2026-548
Preprint. Discussion started: 9 April 2026

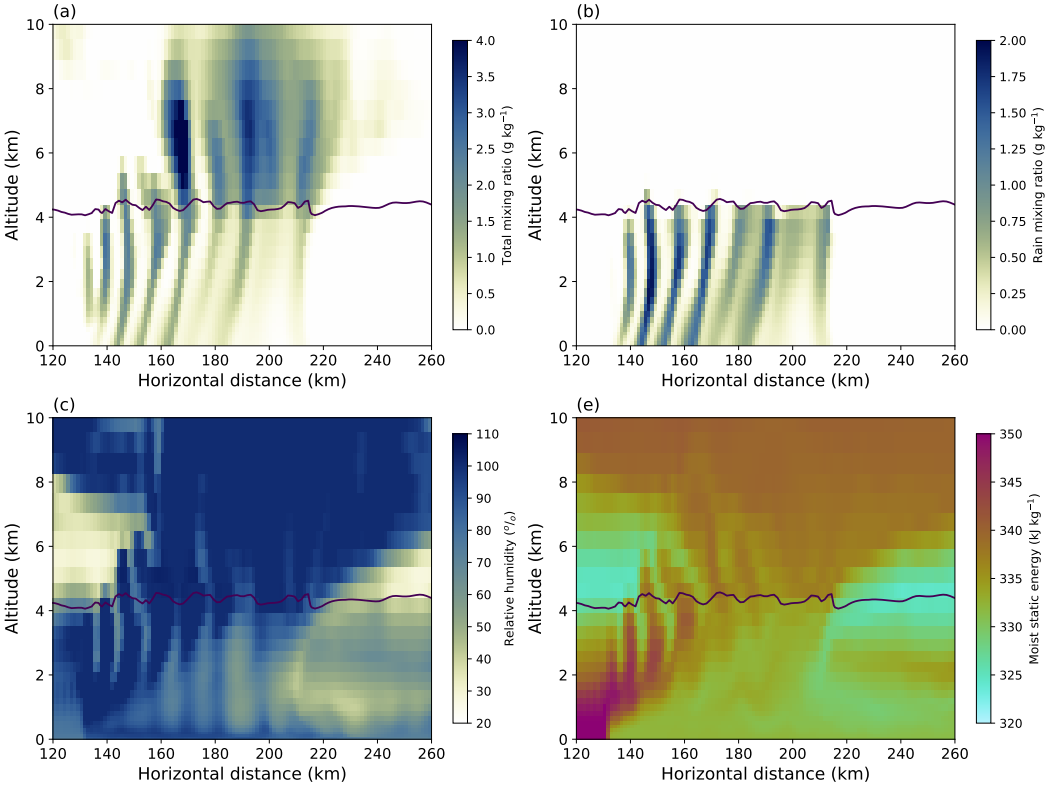

Figure 4. Vertical cross section of the (a) total condensed water mixing ratio ($\mathrm{g\,kg^{-1}}$), (b) rain mixing ratio (($\mathrm{g\,kg^{-1}}$), (c) relative humidity (%) and (d) moist static energy ($\mathrm{kj\,kg^{-1}}$) after 6 hours. The black line corresponds to the $0^{\circ}\mathrm{C}$ isotherm.

4.5 Isotopic results after 6 hours of simulation

Updrafts in the convective zone are transient, i.e. their exact location varies with time (not shown). Thus, rather than calculating temporal averages when the squall line is most intense, we analyze snapshots at a given time step. In the following, we chose to show results after 6 hours of simulation as we can clearly distinguish between the convective and stratiform zones as described in the previous section. We checked that results are qualitatively similar whatever the snapshot we chose during the time interval of 5 to 6 hours. Although the stratiform zone is in development earlier in the simulation, we also show isotopic results after 4 hours of simulation in the supplementary material to show that (1) the non isotopic steady state has no impact on results and (2) the expected isotopic characteristics are well reproduced elsewhere in the simulation with a squall line at a different stage of development.

To document the isotopic results, we plot two figures. Figure 6a-d shows the cross section of anomalies of the isotopic composition (δ^{18}O and d-excess) of both water phases. The isotopic anomalies are relative to the domain-mean at each level. We also show on Fig. 6e the difference between the isotopic composition of rain ($\delta^{18}\mathrm{O}_p$) and the isotopic composition of rain in equilibrium with water vapor (($\delta^{18}\mathrm{O}_p)_{eq}$), hereafter named the isotopic disequilibrium for δ^{18}O ($\delta^{18}\mathrm{O}_p - (\delta^{18}\mathrm{O}_p)_{eq}$). A

https://doi.org/10.5194/egusphere-2026-548
Preprint. Discussion started: 9 April 2026

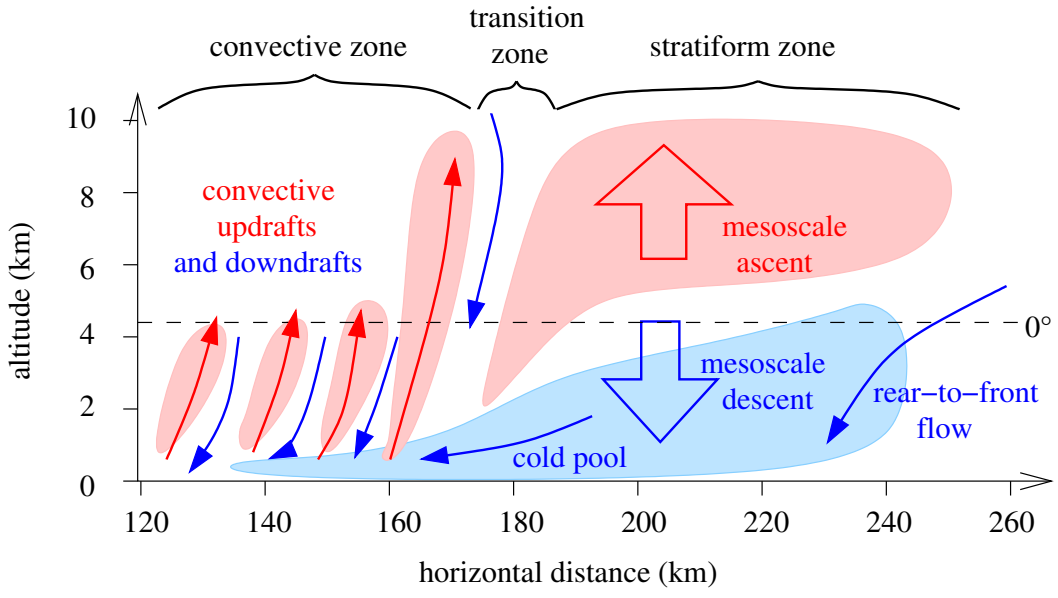

Figure 5. Schematic of the main structural components of a squall line moving from right to left with the three convective, transition and stratiform zones along with horizontal and vertical dynamic.

similar disequilibrium is calculated for d-excess (d-excess$_p$ - (d-excess$_p$)$_{eq}$) and shown on Fig. 6f. The absolute isotopic values are shown on Fig. S2a-d in supplementary material. Fig. 7 shows the isotopic composition of both water phases at the surface along the x-direction.

4.5.1 Description of the isotopic variations in the 2D domain

In the convective zone, we clearly distinguish on Fig. 6a the previously identified updrafts with enriched water vapor exported from the surface layer and, in between, downdrafts with lower $\delta^{18}O_v$ probably reflecting export of depleted water vapor from higher altitude. We also probably detect rain evaporation within downdrafts, where the rain evaporation preferentially occurs, with narrow vertical plumes of higher $\delta^{18}O_p$ (see Fig. 6b and red color on Fig. S2b from 1 to 3.5 km) and lower d-excess$_p$ (see Fig. 6d and orange color on Fig. S2d from 1 to 3.5 km) consistent with previous studies (Kurita, 2013; Risi et al., 2021, 2010). The lower d-excess$_p$ when evaporation processes are at play is interpreted as the kinetic effects during rain evaporation: HD^{16}O diffuses more than 8 times faster than the $H_2^{18}O$ lowering deuterium excess in precipitation. The rain evaporation in narrow downdrafts is also suggested by positive (negative) isotopic disequilibrium for $\delta^{18}O_p$ (d-excess$_p$) (Fig. 6e-f) (rain evaporation leads rain to be more enriched than expected at isotopic equilibrium and d-excess$_p$ to be lower than expected at isotopic equilibrium). Both vertical motions and rain evaporation in the convective zone can be seen also in d-excess$_v$ (Fig. 6c and Fig. S2c). The lower d-excess$_v$ in updrafts suggests the export of low d-excess$_v$ from the surface layer toward higher altitude. The

https://doi.org/10.5194/egusphere-2026-548
Preprint. Discussion started: 9 April 2026

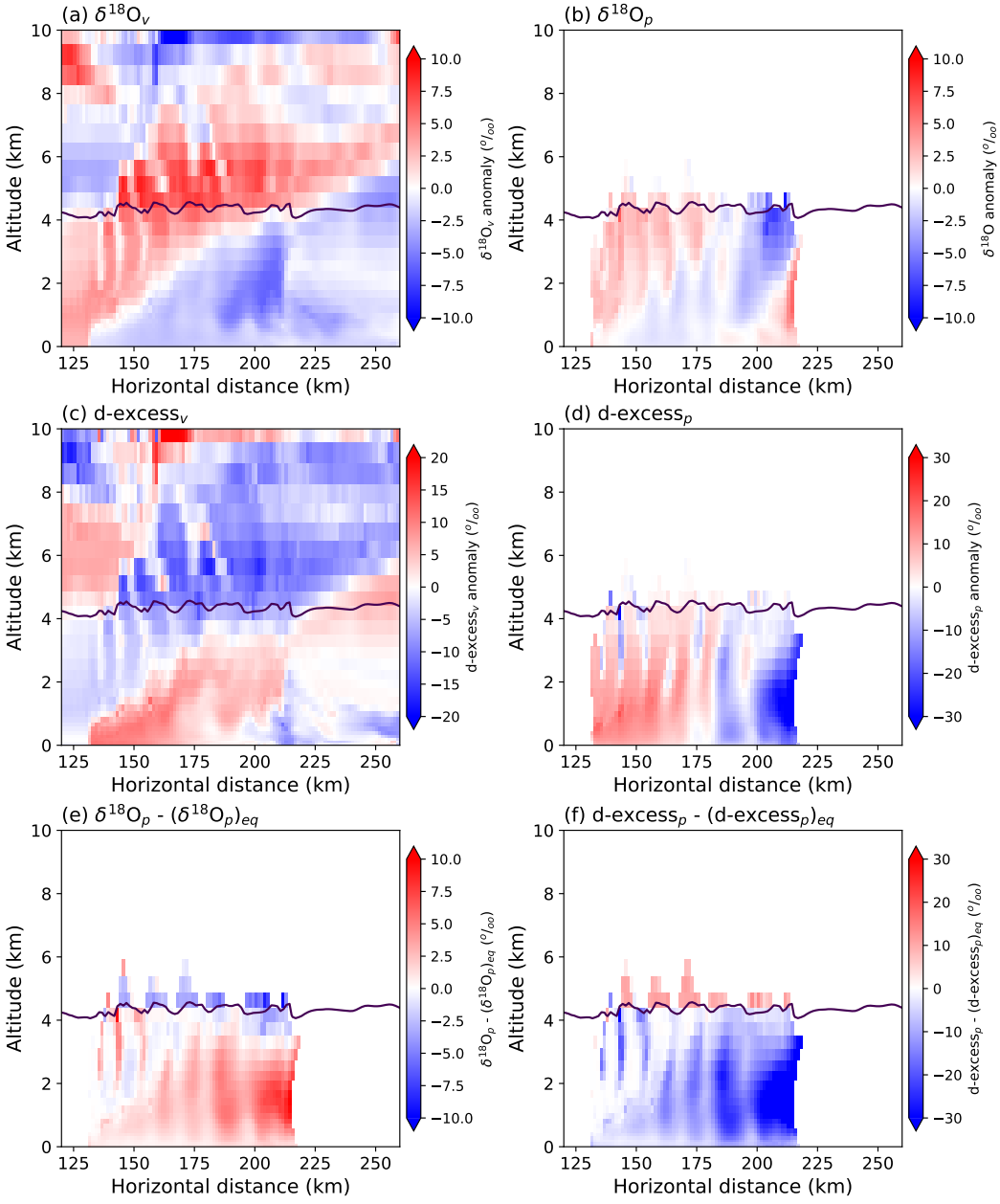

Figure 6. Vertical cross section after 6 hours of (a) $\delta^{18}O_v$, (b) $\delta^{18}O_p$, (c) d-excess$_v$,(d) d-excess$_p$, (e) $\delta^{18}O_p$ - $(\delta^{18}O_p)_{eq}$ and (f) d-excess$_p$ - (d-excess$_p$)$_{eq}$. Panels (a) to (d) are anomalies calculated by subtracting the average value of the variable at a given altitude from the local value of the variable. The black line corresponds to the 0°C isotherm.

higher d-excess$_v$ in downdrafts is likely related to rain evaporation (under strong rain, a low fraction of rain evaporation tends to increase d-excess$_v$) and to air subsidence exporting higher d-excess$_v$ from higher altitude.

https://doi.org/10.5194/egusphere-2026-548
Preprint. Discussion started: 9 April 2026

In the stratiform zone, under the anvil cloud, the water vapor is more depleted in average than in the convective zone (Fig. 6a) as expected from the progressive depletion of water vapor by rain evaporation, meso-scale downdrafts and higher condensation altitude (Aggarwal et al., 2016; Kurita, 2013; Risi et al., 2021). We can see lower values of $\delta^{18}O_p$ at around 210 km and above 3 km (Fig. 6b and S2b). This could reflect that rain originates from snow melt, which is more depleted than the rain that would has formed locally because the snow has formed at higher altitude as already suggested by Risi et al. (2010, 2021). This is in agreement with the negative disequilibrium for $\delta^{18}O_p$ in this area (Fig. 6e and S2e). In contrast, between 200 and 215 km and below 3 km, $\delta^{18}O_p$ is higher and d-excess$_p$ is lower (actually negative, see Fig. S2d) down to the surface (Fig. 6b-d and S2b-d) probably reflecting the enriched effect of rain evaporation on $\delta^{18}O_p$ and the lowering effect on d-excess$_p$, consistently with the positive (negative) disequilibrium for $\delta^{18}O_p$ (d-excess$_p$) in this area (Fig. 6e-f and S2e-f). The impact of rain evaporation is also seen on $\delta^{18}O_v$ in this part of the domain (Fig. 6a) with the expected depleted effect on $\delta^{18}O_v$. The expected higher d-excess$_v$ is also seen between 200 and 215 km but in a restricted region between 0.5 to 2.5 km height (Fig. 6c and S2c).

In the transition zone, the expected isotopic characteristics are more visible on the precipitation phase and on Fig. S2. We identify in the three dry air patches shown on Fig. 4c (roughly located at 165, 175 and 190 km) both higher values of $\delta^{18}O_p$ and lower values of d-excess$_p$ (Fig. S2b-d) suggesting that evaporation processes are at play, consistently with strong positive (negative) disequilibrium for $\delta^{18}O_p$ (d-excess$_p$) (Fig. 4e-f).

4.5.2 Description of temporal evolution of the surface isotopic composition

Our simulation exhibits four precipitation maxima in the convective zone corresponding to the aforementioned convective updrafts, followed by lower precipitation in the transition region with two peaks (Fig. 7a). Two precipitation peaks are also seen in the stratiform region: the first one located at 195 km is attributed to stratiform rain as the later falls diagonally toward the front of the system as shown on Fig. 4b. This is consistent with surface observations although usually only one convective precipitation maximum is found (Risi et al., 2010).

Our simulation shows a W-shaped $\delta^{18}O_p$ (Fig. 7b, blue lines). Two local isotopic minimums are observed in the convective zone and at the onset of stratiform region at about 160 km and 195 km respectively. In the transition region, the peak in the middle of the W is actually formed in our simulation by a double-isotopic peaks (at around 175 and 190 km). This W-shape has often been observed in the isotopic composition of precipitation of squall lines (Rindsberger et al., 1990; Risi et al., 2010; Taupin and Gallaire, 1998). Typically, $\delta^{18}O_p$ in our simulation can be compared to the isotopic variations observed in precipitation collected along the squall line that occurred on August 18th, 2006 in Niamey (see Fig. 2 in Risi et al. (2010)).

Regarding the simulated $\delta^{18}O_v$, there is a sharp decrease right after 130 km corresponding to the cold pool front which is observed for more than 85% of squall lines in Niamey from 2010 to 2012 (Tremoy et al., 2014). Then, $\delta^{18}O_v$ decreases along the convective zone before slightly increasing (about 1 ‰) in the transition and stratiform zones as observed in about 30% of squall in Tremoy et al. (2014).

According to previous studies dealing with conceptual and cloud resolving models (Risi et al., 2021, 2023), the main processes depleting near-surface water vapor in convective and stratiform zones are mesoscale descents, rain evaporation in a moist environment, and enhanced rain-water vapor diffusive exchanges (as rain falls into layers that are more and more enriched, dif-

https://doi.org/10.5194/egusphere-2026-548
Preprint. Discussion started: 9 April 2026

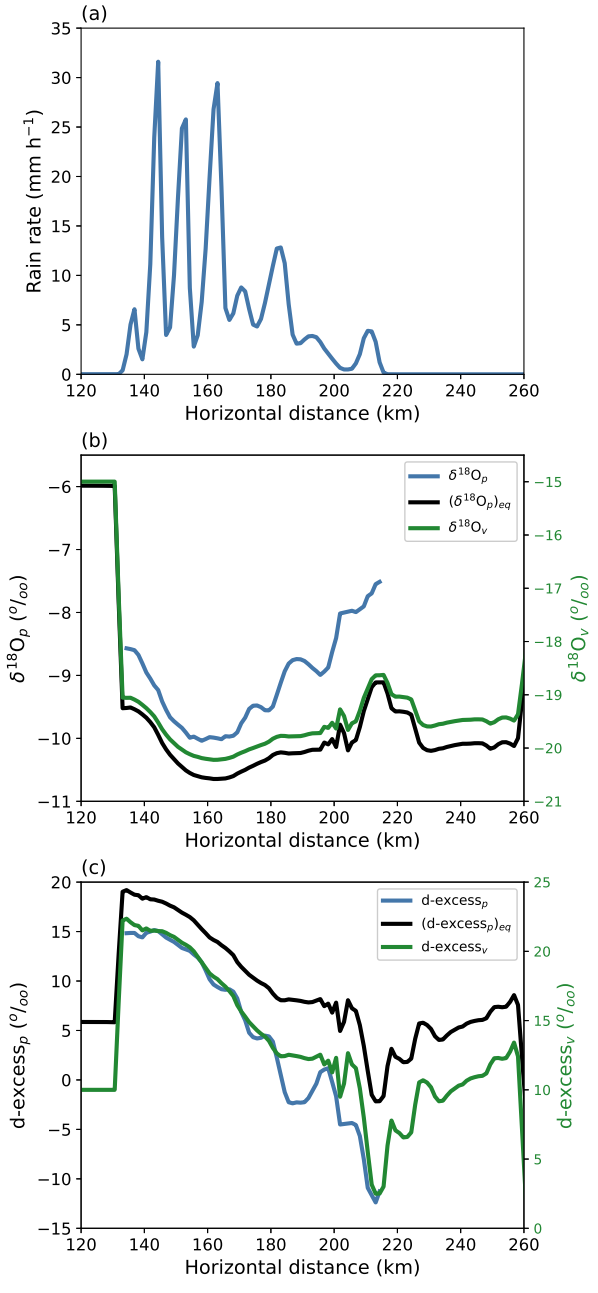

Figure 7. Evolution of the surface rain rate (a), $\delta^{18}O$ (b), and and d-excess (c) along the x-direction after 6 hours of simulation. In (b) and (c), the blue, black and green lines correspond to the isotopic composition of rain, rain in isotopic equilibrium with water vapor, and water vapor, respectively. In (b) and (c), the isotopic composition of rain (water vapor) is on the left-y (right-y) axis.

https://doi.org/10.5194/egusphere-2026-548
Preprint. Discussion started: 9 April 2026

fusive exchanges tend to enrich the precipitation and deplete water vapor around it). The isotopic decrease in precipitation along the convective zone follows to first order that in the water vapor, both phases being in close equilibrium at the surface (Fig. 7b, black lines).

The decreasing trend in $\delta^{18}O_p$ is however interrupted from the transition zone. Superimposed on the increasing $\delta^{18}O_p$ trend, the two peaks that form the middle of the W reflect the enrichment of rain by evaporation during its fall in dry air (Fig. 4c) as suggested by Risi et al. (2010). Rain is always enriched by evaporation processes but the drier the air, the more enriching evaporation is for a constant fraction of evaporated rain.

The $\delta^{18}O_p$ recovery after 195 km, corresponding to the right limb of the W-shaped pattern, is attributed to increasing evaporative enrichment in the stratiform zone in a drier environment (Risi et al., 2010; Tremoy et al., 2014; Risi et al., 2023) (see also next section).

Deuterium excess in precipitation continuously falls along the simulated squall line and attains strong negative values (-10 ‰) after 210 km during the second precipitation peak in the stratiform zone (Fig. 7c, blue lines) as observed for some squall lines in Risi et al. (2010). This is consistent with rain evaporation aforementioned increasing from the transition zone. We also observe two decreases in d-excess$_p$ in the transition region in phase with the $\delta^{18}O_p$ double peaks consistently with rain evaporation. Deuterium excess in water vapor also decreases along the squall line as observed by Tremoy et al. (2014) for more than 85% of observed squall lines.

It is worth noting that the effect of rain evaporation on isotopic results at the surface could be reduced because of the presence of a humid surface layer (Fig. 4c) leading to first order to isotopic equilibrium between rain and water vapor (Fig. 7, black lines). Diffusive exchanges are thus favored instead of rain evaporation. This could explain for example that higher d-excess$_v$ is not seen under strong rain (low fraction of rain evaporation increases d-excess$_v$).

4.5.3 Analysis of the rain evaporation processes

Figure 8a shows the disequilibrium for $\delta^{18}O_p$ at different altitudes (surface, 1 km and 4 km). Positive values mean that the rain is more enriched than if it was at equilibrium with water vapor, reflecting evaporative processes. Negative values mean that the rain is more depleted than if it was at equilibrium with water vapor, reflecting rain falling from higher altitude and further depleted.

At 4 km altitude, rain is more depleted than expected from isotopic equilibrium with water vapor, meaning that it falls from higher altitude (Fig. 8a). This phenomenon increases with the x-direction, reflecting the transition from the convective to the stratiform region, where condensation occurs higher (Fig. 4a). At 1 km, rain is more enriched than expected from equilibrium with water vapor, reflecting evaporative enrichment. This phenomenon increases with x-direction, reflecting the drier and drier air in the mesoscale descent under the anvil. At the surface, the disequilibrium for $\delta^{18}O_p$ is still positive but lower than at 1 km. The rain is closer to the isotopic equilibrium with the vapor. This is likely due to the presence of an excessive humid surface layer near the surface as mentioned above (Fig. 4a).

The same phenomenon is at play for deuterium excess (Fig. 8b). At 4 km altitude, the rain has a higher d-excess$_p$ than if at equilibrium with water vapor, because the rain falls from higher altitude and d-excess$_v$ typically increases with altitude (Fig.

https://doi.org/10.5194/egusphere-2026-548
Preprint. Discussion started: 9 April 2026

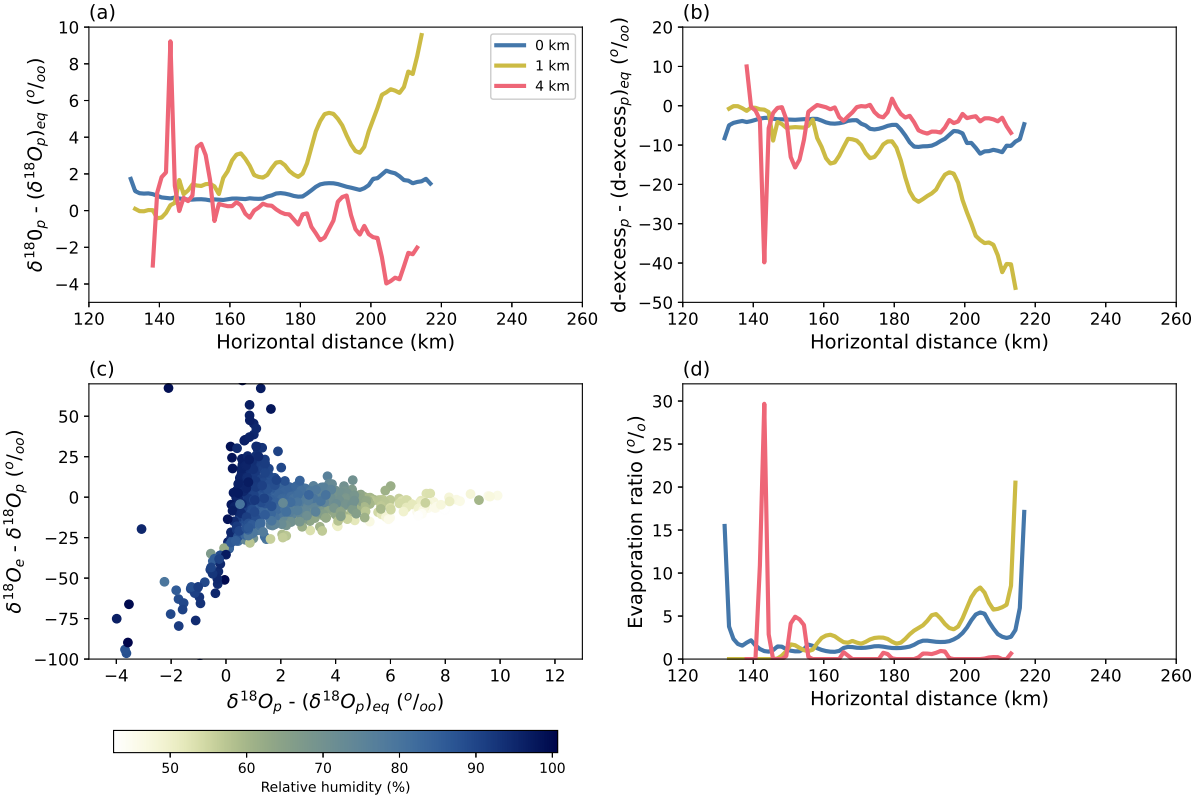

Figure 8. Difference between the isotopic composition of the rain and of the rain at isotopic equilibrium with the vapor at different altitudes for δ^{18}O (a) and d-excess (b) along the x-direction after 6 hours of simulation. (c) Scatter plot of the difference between the δ^{18}O in the evaporation flux and in the rain ($\delta^{18}\mathrm{O_e} - \delta^{18}\mathrm{O}_p$), as a function of the δ^{18}O in the rain and in the vapor at isotopic equilibrium ($\delta^{18}\mathrm{O}_p - (\delta^{18}\mathrm{O}_p)_{\mathrm{eq}}$), for all x-values and altitudes where rain occurs. Markers are colored by relative humidity. (d) Fraction of rain that evaporates along the x-direction after 6 hours of simulation at different altitudes. The blue, golden and red lines correspond to the isotopic composition at the surface, 1 km altitude and 4 km altitude, respectively.

S2c). At 1 km height, the rain has a smaller d-excess$_p$ due to the impact of rain evaporation that enhances with x-direction (Fig. S2d). At surface, the disequilibrium for d-excess$_p$ is slightly negative but we can not exclude that the humid surface layer reduces this disequilibrium through diffusive exchanges between both water phases.

The processes controlling the disequilibrium between rain and water vapor are illustrated in Fig. 8c, showing the difference between the δ^{18}O in the evaporation flux and in the rain ($\delta^{18}\mathrm{O}_e - \delta^{18}\mathrm{O}_p$), as a function of the disequilibrium for $\delta^{18}\mathrm{O}_p$ for all x-values and altitudes where rain occurs. Where relative humidity is high (dark blue shades), any small disequilibrium between rain and water vapor implies diffusive exchanges between both phases to bring them in equilibrium. For example, if rain is more depleted than expected (negative $\delta^{18}\mathrm{O}_p - (\delta^{18}\mathrm{O}_p)_{eq}$), then $\delta^{18}\mathrm{O}_e$ is much more depleted than $\delta^{18}\mathrm{O}_p$ to bring rain and water vapor to equilibrium. As a result, rain and water vapor are close to equilibrium (near-zero $\delta^{18}\mathrm{O}_p - (\delta^{18}\mathrm{O}_p)_{eq}$). In contrast,

https://doi.org/10.5194/egusphere-2026-548
Preprint. Discussion started: 9 April 2026

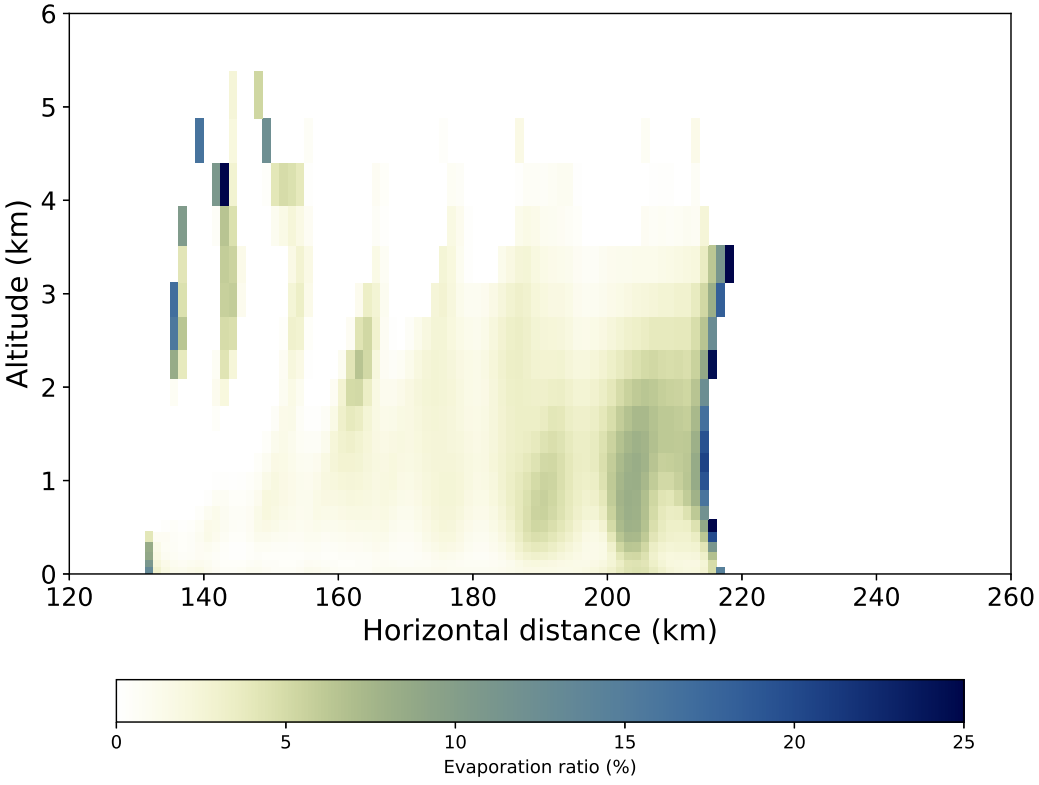

Figure 9. Vertical cross section of the fraction of rain that evaporates (%) at 6 hours.

where relative humidity is small (beige shades), the fraction of rain that evaporates is large, and thus the evaporation flux has almost the same δ^{18}O as rain (near-zero values of $\delta^{18}O_e - \delta^{18}O_p$). The strong evaporation leads to evaporative enrichment of rain (high values of $\delta^{18}O_p - (\delta^{18}O_p)_{eq}$). This behavior is expected, giving us confidence in our implementation of isotopic processes associated with rain evaporation.

As a first exploration, we defined a rough estimate of the evaporated fraction of rain in the model. We show on Fig. 8d and 9 the ratio between the tendency of rain evaporation (evaporation flux derivative as a function of time) and the mixing ratio of rain. This ratio is the rain-normalized evaporated fraction of rain in each grid (0% means that no evaporation occurred, 100% means that all rain evaporated):

$$R_{\mathrm{EVA}} = \frac{\Delta r|_{\mathrm{EVA}} \times dt}{r_r} \times 100 \tag{33}$$

with dt the model time step.

In the convective zone, evaporation occurs in the narrow dry downdrafts between 2 and 4.5 km height and evaporation rate can attain up to around 30% in a few grids (Fig. 8d and 9). In the transition zone, rain evaporation is present within the dry patches of subsiding air from about 500 m to 3.5 km with an evaporation rate varying between 0 and 10% at a given level. At

https://doi.org/10.5194/egusphere-2026-548
Preprint. Discussion started: 9 April 2026

last, Fig. 8d and 9 clearly show that rain evaporation is present almost all over the domain under the anvil cloud and reaches a maximum at the edge of the stratiform zone (at about 215 km) where evaporation rate attains close to 30% all along the vertical dimension from the near-surface to 3.5 km height. This 2D spatial pattern of the evaporative rate is consistent with the spatial isotopic variations of water vapor and precipitation, giving us confidence again in our implementation of isotopic processes associated with rain evaporation. However, it is worth noting that the estimates for the evaporated fraction of rain in the model are given for one altitude and thus are lower than ones previously published because the later further reflected a cumulated evaporation rate of the droplets through its fall. Based on a box model aiming at reproducing the near-surface observations, Tremoy et al. (2014) concluded that for a majority of squall lines, the rain evaporation rate varies between 10 and 35% with a maximum at the rear of the stratiform zone that can attain almost 60% in a few cases. Using cloud resolving model in radiative-convective equilibrium to simulate an idealized squall line, Risi et al. (2023) simulated a similar range for the rain evaporation rate in the convective and stratiform zones, increasing up to 90 % in the trailing environment.

5 Conclusions

This paper presents the implementation of water stable isotopes in the non-hydrostatic mesoscale model Meso-NH. This development is tested with the simulation of a squall line that occurred at night on June 23-24, 1981 during the COPT81 intensive field campaign. We chose this squall line as it was fully observed on the field and as a 2D simulation was done by Caniaux et al. (1994) with Meso-NH. Our simulation successfully reproduces the main expected spatial structure of a mature and intense squall line after 6 hours of simulation : a convective zone, a transition zone and a stratiform zone where different processes are expected to produce different isotopic fractionation on water vapor and precipitation.

It is worth noting that despite the non-isotopic steady state of the near-surface water vapor after 8 hours of simulation, the isotopic results are actually consistent with observations after 6 hours of simulation. This is also the case earlier in the simulation as shown for example after 4 hours of simulation when the convective zone is formed and the stratiform region on development (Fig. S3 to S7). This result suggests that the non-isotopic steady state in near-surface water vapor at the end of the simulation is a minor problem to explore the isotopic variations of water in our simulation.

The Meso-NH-ISO model well captures the main isotopic features expected as seen in many observations:

- Regarding the spatial pattern of the isotopic composition of water in the 2D domain: (i) In the convective zone, our simulation well reproduces the enriched and depleted water vapor in updrafts and downdrafts respectively reflecting both vertical motions of water and rain evaporation processes. (ii) In the transition zone, the impact of rain evaporation processes on the isotopic composition of precipitation is also well reproduced in the dry plumes of subsiding air with an enrichment of $\delta^{18}O_p$, low - even negative - values of d-excess$_p$ and a positive disequilibrium for $\delta^{18}O_p$. (iii) In the stratiform zone, our simulation captures the expected processes. The low $\delta^{18}O_p$ in altitude reflects the higher altitude of condensation in this zone. The negative values of d-excess$_p$ and the highest values of $\delta^{18}O_p$ below the anvil cloud reflect rain evaporation processes, specifically at the rear of the stratiform zone where our estimate of the fraction of rain

https://doi.org/10.5194/egusphere-2026-548
Preprint. Discussion started: 9 April 2026

that evaporates is the stronger. The analysis of evaporation processes in our simulation shows that these processes act as expected in modulating the isotopic composition of water in the 2D domain.

- Regarding the comparison with the observations of the isotopic composition of water at the surface: (i) Along the squall line, $\delta^{18}O_p$ evolves along a W-shaped pattern as observed for numerous squall lines by Rindsberger et al. (1990); Taupin and Gallaire (1998); Risi et al. (2010). The increasing $\delta^{18}O_p$ in the middle of the W and at the end of the W, attributed in previous studies to rain evaporation in a drier environment in the transition zone and at the rear of the stratiform zone, are well reproduced in our simulation (ii) $\delta^{18}O_v$ decreases along the convective zone before slightly increasing in the transition and stratiform zones as observed in about 30% of squall lines in Tremoy et al. (2014). The lowering of $\delta^{18}O_v$ has been explained in previous studies as reflecting mesoscale descents, rain evaporation and favored diffusive exchange between rain and water vapor in moist environment. (iii) Deuterium excess in precipitation and water vapor decreases along the squall line as already observed in Risi et al. (2010) and Tremoy et al. (2014) respectively that is consistent with rain evaporation, mesoscale descents and presence of a enhanced diffusive exchanges at surface.

The perspective of this implementation is to use Meso-NH-ISO for realistic cases of squall lines and cyclones in order to better understand what are the controls on the isotopic composition of water in convective systems. For example, Vimeux et al. (2024) recently showed the presence of a very organized signal in the isotopic composition of water vapor within cyclones on an hourly scale, empirically linked to the spatial structure of cyclones. Observations alone and general atmospheric climate models, even with a high spatial resolution, have not been able to decipher the processes controlling isotopic variations in water vapor and therefore to quantify them. Future simulations with Meso-NH-ISO should enable further advances on this aspect with the final objective of better studying and quantifying convective processes from water stable isotopes.

Code availability. The water isotopes scheme has been implemented in the 5.5 version of the Meso-NH code. This reference version is under the CeCILL-C license agreement and freely available at http://mesonh.aero.obs-mip.fr/mesonh55). The complete code of Meso-NH v5-5-0 including the water isotope scheme is available at https://doi.org/10.5281/zenodo.18428400 (Barthe, 2026). This repository also contains namelists to run the 2D squall line and Python scripts to reproduce the figures of this manuscript.

Author contributions. CB and SF developed the implementation of water stable isotopes in Meso-NH. FV and CR interpreted the isotopic results. CB, FV and CR wrote the paper. CB realized figures and tables.

Competing interests. The contact author has declared that none of the authors has any competing interests

https://doi.org/10.5194/egusphere-2026-548
Preprint. Discussion started: 9 April 2026

Acknowledgements. This work was funded by the French CNRS-INSU national program LEFE (project MISO-CYCLO) and the ANR PALEOTEMPESTO proposal 24-CE01-6978. The work benefited from a PhD grant from the CEA. Computations were performed on the 120-node cluster of Laboratoire d'Aérologie.

https://doi.org/10.5194/egusphere-2026-548
Preprint. Discussion started: 9 April 2026

References

Aggarwal, P. K., Romatschke, U., Araguas-Araguas, L., Belachew, D., Longstaffe, F. J., Berg, P., Schumacher, C., and Funk, A.: Proportions of convective and stratiform precipitation revealed in water isotope ratios, Nat. Geosci., 9, 624–629, https://doi.org/10.1038/ngeo2739, 2016.

Arnault, J., Jung, G., Haese, B., Fersch, B., Rummler, T., Wei, J., Zhang, Z., and Kunstmann, H.: A Joint Soil-Vegetation-Atmospheric Modeling Procedure of Water Isotopologues: Implementation and Application to Different Climate Zones With WRF-Hydro-Iso, J. Adv. Model. Earth Sy., 13, e2021MS002 562, https://doi.org/10.1029/2021MS002562, 2021.

Barthe, C.: Water isotope scheme in MesoNH-V5-5-0, https://doi.org/10.5281/zenodo.18428400, zenodo [code], 2026.

Barthe, C., Chong, M., Pinty, J.-P., Bovalo, C., and Escobar, J.: CELLS v1. 0: updated and parallelized version of an electrical scheme to simulate multiple electrified clouds and flashes over large domains., Geosci. Model Dev., 5, 167–184, https://doi.org/10.5194/gmd-5-167-2012, 2012.

Bechtold, P., Bazile, E., Guichard, F., Mascart, P., and Richard, E.: A mass-flux convection scheme for regional and global models, Q. J. Roy. Meteor. Soc., 127, 869–886, https://doi.org/10.1002/qj.49712757309, 2001.

Blossey, P. N., Kuang, Z., and Romps, D. M.: Isotopic composition of water in the tropical tropopause layer in cloud-resolving simulations of an idealized tropical circulation, J. Geophys. Res., 115, https://doi.org/10.1029/2010JD014554, 2010.

Bony, S., Risi, C., and Vimeux, F.: Influence of convective processes on the isotopic composition (δ^{18}O and δD) of precipitation and water vapor in the Tropics. Part 1: Radiative-convective equilibrium and TOGA-COARE simulations, J. Geophys. Res. Atmos., 113, https://doi.org/10.1029/2008JD009942, 2008.

Caniaux, G., Redelsperger, J.-L., and Lafore, J.-P.: A Numerical Study of the Stratiform Region of a Fast-Moving Squall Line. Part I: General Description and Water and Heat Budgets, J. Atmos. Sci., 51, 2046–2074, https://doi.org/10.1175/1520-0469(1994)0512.0.CO;2, 1994.

Chakraborty, S., Sinha, N., Chattopadhyay, R., Sengupta, S., Mohan, P., and Datye, A.: Atmospheric controls on the precipitation isotopes over the Andaman Islands, Bay of Bengal, Sci. Rep., 6, 1–11, https://doi.org/10.1038/srep19555, 2016.

Chalon, J.-P., Jaubert, G., Lafore, J.-P., and Roux, F.: The West African Squall Line Observed on 23 June 1981 during COPT81: Mesoscale Structure and Transports, J. Atmos. Sci., 45, 2744–2763, https://doi.org/10.1175/1520-0469(1988)045<2744:TWASLO>2.0.CO;2, 1988.

Chang, C.-Y. and Yoshizaki, M.: Three-Dimensional Modeling Study of Squall Lines Observed in COPT81, J. Atmos. Sci., 50, 161–183, https://doi.org/10.1175/1520-0469(1993)0502.0.CO;2, 1993.

Chong, M., Amayenc, P., Scialom, G., and Testud, J.: A Tropical Squall Line Observed during the COPT 81 Experiment in West Africa. Part 1: Kinematic Structure Inferred from Dual-Doppler Radar Data, Mon. Wea. Rev., 115, 670–694, https://doi.org/10.1175/1520-0493(1987)1152.0.CO;2, 1987.

Cohard, J.-M. and Pinty, J.-P.: A comprehensive two-moment warm microphysical bulk scheme. I: Description and tests, Q. J. Roy. Meteor. Soc., 126, 1815–1842, https://doi.org/10.1002/qj.49712656613, 2000.

Cruz, F. W., Vuille, M., Burns, S. J., Wang, X., Cheng, H., Werner, M., Edwards, R. L., Karmann, I., Auler, A. S., and Nguyen, H.: Orbitally driven east-west antiphasing of South American precipitation, Nat. Geosci., 2, 210–214, https://doi.org/10.1038/ngeo444, 2009.

Cuxart, J., Bougeault, P., and Redelsperger, J.-L.: A turbulence scheme allowing for mesoscale and large-eddy simulations, Q. J. Roy. Meteor. Soc., 126, 1–30, https://doi.org/10.1002/qj.49712656202, 2000.

Dansgaard: Stable isotopes in precipitation, Tellus, 16, 436–468, https://doi.org/10.3402/tellusa.v16i4.8993, 1964.

https://doi.org/10.5194/egusphere-2026-548
Preprint. Discussion started: 9 April 2026

Dubos, T., Dubey, S., Tort, M., Mittal, R., Meurdesoif, Y., and Hourdin, F.: DYNAMICO-1.0, an icosahedral hydrostatic dynamical core designed for consistency and versatility, Geosci. Model Dev., 8, 3131–3150, https://doi.org/10.5194/gmd-8-3131-2015, 2015.

Gamache, J. F. and Houze, R. A.: Mesoscale air motions associated with a tropical squall line, Mon. Wea. Rev., 110, 118–135, https://doi.org/10.1175/1520-0493, 1981.

Hall, W. D. and Pruppacher, H. R.: The Survival of Ice Particles Falling from Cirrus Clouds in Subsaturated Air, J. Atmos. Sci., 33, 1995–2006, https://doi.org/10.1175/1520-0469(1976)0332.0.CO;2, 1976.

Hanisco, T., Moyer, E., Weinstock, E., St Claire, J. M., Sayres, D. S., Smith, J. B., Lockwood, R., Anderson, J. G., Dessler, A. E., Keutsh, F. N., Spackman, J. R., Read, W. G., and Bui, T. P.: Observations of deep convective influence on stratospheric water vapor and its isotopic composition, Geophys. Res. Lett., 34, https://doi.org/10.1029/2006GL027899, 2007.

Hogan, R. J. and Bozzo, A.: A Flexible and Efficient Radiation Scheme for the ECMWF Model, J. Adv. Model. Earth Sy., 10, 1990–2008, https://doi.org/10.1029/2018MS001364, 2018.

Hourdin, F., Rio, C., Grandpeix, J.-Y., Madeleine, J.-B., Cheruy, F., Rochetin, N., Jam, A., Musat, I., Idelkadi, A., Fairhead, L., et al.: LMDZ6A: The atmospheric component of the IPSL climate model with improved and better tuned physics, J. Adv. Model. Earth Sy., 12, e2019MS001 892, https://doi.org/10.1029/2019MS001892, 2020.

Houze, R. A.: Structure and dynamics of a tropical squall line system, Mon. Wea. Rev., 105, 1540–1567, https://doi.org/10.1175/1520-0493(1977)105<1540:SADOAT>2.0.CO;2, 1977.

Jouzel, J. and Merlivat, L.: Deuterium and oxygen 18 in precipitation: Modeling of the isotopic effects during snow formation, J. Geophys. Res. Atmos., 89, 11 749–11 757, https://doi.org/10.1029/JD089iD07p11749, 1984.

Kessler, E.: On the Distribution and Continuity of Water Substance in Atmospheric Circulations, p. 1–84, American Meteorological Society, Boston, MA, https://doi.org/10.1007/978-1-935704-36-2_1, 1969.

Kurita, N.: Water isotopic variability in response to mesoscale convective system over the tropical ocean, J. Geophy. Res. Atmos., 118, 10,376–10,390, https://doi.org/10.1002/jgrd.50754, 2013.

Lac, C., Chaboureau, J.-P., Masson, V., Pinty, J.-P., Tulet, P., Escobar, J., Leriche, M., Barthe, C., Aouizerats, B., Augros, C., Aumond, P., Auguste, F., Bechtold, P., Berthet, S., Bielli, S., Bosseur, F., Caumont, O., Cohard, J.-M., Colin, J., Couvreux, F., Cuxart, J., Delautier, G., Dauhut, T., Ducrocq, V., Filippi, J.-B., Gazen, D., Geoffroy, O., Gheusi, F., Honnert, R., Lafore, J.-P., Lebeaupin Brossier, C., Libois, Q., Lunet, T., Mari, C., Maric, T., Mascart, P., Mogé, M., Molinié, G., Nuissier, O., Pantillon, F., Peyrillé, P., Pergaud, J., Perraud, E., Pianezze, J., Redelsperger, J.-L., Ricard, D., Richard, E., Riette, S., Rodier, Q., Schoetter, R., Seyfried, L., Stein, J., Suhre, K., Taufour, M., Thouron, O., Turner, S., Verrelle, A., Vié, B., Visentin, F., Vionnet, V., and Wautelet, P.: Overview of the Meso-NH model version 5.4 and its applications, Geosci. Model Dev., 11, 1929–1969, https://doi.org/10.5194/gmd-11-1929-2018, 2018.

Lacour, J.-L., Risi, C., Worden, J., Clerbaux, C., and Coheur, P.-F.: Isotopic signature of convection's depth in water vapor as seen from IASI and TES D observations, Earth Planet. Sci. Lett., 7, 9645–9663, https://doi.org/10.5194/acp-17-9645-2017, 2017.

Lafore, J.-P. and Moncrieff, M. W.: A numerical investigation of the organization and interaction of the convective and startiform regions of tropical squall lines, J. Atmos. Sci., 46, 521–544, https://doi.org/10.1175/1520-0469(1989)046<0521:ANIOTO>2.0.CO;2, 1989.

Lafore, J.-P., Redelsperger, J.-L., and Jaubert, G.: Comparison between a Tree-dimensional simulation and Doppler radar Data of a tropical squall line: transports of mass, momentum, heat and moisture, J. Atmos. Sci., 45, 3483–3500, https://doi.org/10.1175/1520-0469(1988)045<3483:CBATDS>2.0.CO;2, 1988.

https://doi.org/10.5194/egusphere-2026-548
Preprint. Discussion started: 9 April 2026

Lawrence, J. R., Gedzelman, S. D., Dexheimer, D., Cho, H.-K., Carrie, G. D., Gasparini, R., Anderson, C. R., Bowman, K. P., and Biggerstaff, M. I.: Stable isotopic composition of water vapor in the tropics, J. Geophys. Res. Atmos., 109, D06 115, https://doi.org/10.1029/2003JD004046, 2004.

Lee, J.-E., Fung, I., DePaolo, D., and Fennig, C. C.: Analysis of the global distribution of water isotopes using the NCAR atmospheric general circulation model, J. Geophys. Res., 112, D16 306, https://doi.org/10.1029/2006JD007657, 2007.

Leriche, M., Pinty, J.-P., Mari, C., and Gazen, D.: A cloud chemistry module for the 3-D cloud-resolving mesoscale model Meso-NH with application to idealized cases, Geosci. Model Dev., 6, 1275–1298, https://doi.org/10.5194/gmd-6-1275-2013, 2013.

Masson, V., Le Moigne, P., Martin, E., Faroux, S., Alias, A., Alkama, R., Belamari, S., Barbu, A., Boone, A., Bouyssel, F., Brousseau, P., Brun, E., Calvet, J.-C., Carrer, D., Decharme, B., Delire, C., Donier, S., Essaouini, K., Gibelin, A.-L., Giordani, H., Habets, F., Jidane, M., Kerdraon, G., Kourzeneva, E., Lafaysse, M., Lafont, S., Lebeaupin Brossier, C., Lemonsu, A., Mahfouf, J.-F., Marguinaud, P., Mokhtari, M., Morin, S., Pigeon, G., Salgado, R., Seity, Y., Taillefer, F., Tanguy, G., Tulet, P., Vincendon, B., Vionnet, V., and Voldoire, A.: The SURFEXv7.2 land and ocean surface platform for coupled or offline simulation of earth surface variables and fluxes, Geosci. Model Dev., 6, 929–960, https://doi.org/10.5194/gmd-6-929-2013, 2013.

Merlivat, L.: Molecular diffusivities of $H_2^{16}O$, $HD^{16}O$, and $H_2^{18}O$ in gases, J. Chem. Phys., 69, 2864–2871, https://doi.org/10.1063/1.436884, 1978.

Meyers, M. P., DeMott, P. J., and Cotton, W. R.: New Primary Ice-Nucleation Parameterizations in an Explicit Cloud Model, J. Appl. Meteorol. Clim., 31, 708–721, https://doi.org/10.1175/1520-0450(1992)0312.0.CO;2, 1992.

Mlawer, E. J., Taubman, S. J., Brown, P. D., Iacono, M. J., and Clough, S. A.: Radiative transfer for inhomogeneous atmospheres: RRTM, a validated correlated-k model for the longwave, J. Geophys. Res.-Atmos., 102, 16 663–16 682, https://doi.org/10.1029/97JD00237, 1997.

Moore, M., Kuang, Z., and Blossey, P. N.: A moisture budget perspective of the amount effect, Geophys. Res. Lett., 41, 1329–1335, https://doi.org/10.1002/2013GL058302, 2014.

Moore, M., Blossey, P., Muhlbauer, A., and Kuang, Z.: Microphysical controls on the isotopic composition of wintertime orographic precipitation, J. Geophys. Res., 121, 7235–7253, https://doi.org/10.1002/2015JD023763, 2016.

Morcrette, J.-J.: Radiation and cloud radiative properties in the European Centre for Medium Range Weather Forecasts forecasting system, J. Geophys. Res. Atmos., 96, 9121–9132, https://doi.org/10.1029/89JD01597, 1991.

Moyer, E. J., Irion, F. W., Yung, Y. L., and Gunson, M. R.: ATMOS stratospheric deuterated water and implications for troposphere-stratosphere transport, Geophys. Res. Lett., 23, 2385–2388, https://doi.org/10.1029/96GL01489, 1996.

Pergaud, J., Masson, V., Malardel, S., and Couvreux, F.: A Parameterization of Dry Thermals and Shallow Cumuli for Mesoscale Numerical Weather Prediction, Bound.-Lay. Meteorol., 132, 83–106, https://doi.org/10.1007/s10546-009-9388-0, 2009.

Pfahl, S., Wernli, H., Yoshimura, K., and Dubey, M.: The isotopic composition of precipitation from a winter storm–a case study with the limited-area model COSMO iso, Atmos. Chem. Phys., 12, https://doi.org/10.5194/acp-12-1629-2012, 2012.

Pinty, J. P. and Jabouille, P.: A mixed-phase cloud parameterization for use in mesoscale non hydrostatic model: simulations of a squall line and of orographic precipitations, in: Proceedings of Conf. on Cloud Physics, pp. 217–220, Amer. Meteor. Soc Everett, WA, https://worldcat.org/oclc/39920280, 1998.

Pruppacher, H. and Klett, J.: Microphysics of Clouds and Precipitation, Kluwer Academic Publishers, Dordrecht, The Netherlands, https://doi.org/10.1007/978-0-306-48100-0, 1997.

Randall, D., Khairoutdinov, M., Arakawa, A., and Grabowski, W.: Breaking the cloud parameterization deadlock, Bull. Amer. Meteor. Soc., 84, 1547–1564, https://doi.org/10.1175/BAMS-84-11-1547, 2003.

https://doi.org/10.5194/egusphere-2026-548
Preprint. Discussion started: 9 April 2026

Redelsperger, J.-L. and Lafore, J.-P.: A Three-Dimensional Simulation of a Tropical Squall Line: Convective Organization and Thermodynamic Vertical Transport, J. Atmos. Sci., 45, 1334–1356, https://doi.org/10.1175/1520-0469(1988)0452.0.CO;2, 1988.

Riette, S.: Development of "Physical Parametrizations with PYthon" (PPPY, version 1.1) and its usage to reduce the time-step dependency in a microphysical scheme, Geosci. Model Dev., 13, 443–460, https://doi.org/10.5194/gmd-13-443-2020, 2020.

Rindsberger, M., Jaffe, S., Rahamim, S., and Gat, R.: Patterns of the isotopic composition of precipitation in time and space: data from the Israeli storm water collection program, Tellus B, 42, 263–271, https://doi.org/10.3402/tellusb.v42i3.15218, 1990.

Risi, C., Bony, S., and Vimeux, F.: Influence of convective processes on the isotopic composition (δ^{18}O and δD) of precipitation and water vapor in the Tropics: Part 2: Physical interpretation of the amount effect, J. Geophys. Res. Atmos., 113, D19 306, https://doi.org/10.1029/2008JD009943, 2008a.

Risi, C., Bony, S., Vimeux, F., Descroix, L., Ibrahim, B., Lebreton, E., Mamadou, I., and Sultan, B.: What controls the isotopic composition of the African monsoon precipitation? Insights from event-based precipitation collected during the 2006 AMMA campaign, Geophys. Res. Lett., 35, https://doi.org/10.1029/2008GL035920, 2008b.

Risi, C., Bony, S., Vimeux, F., Chong, M., and Descroix, L.: Evolution of the water stable isotopic composition of the rain sampled along Sahelian squall lines, Quart. J. Roy. Meteor. Soc., 136, 227 – 242, https://doi.org/10.1002/qj.485, 2010.

Risi, C., Muller, C., and Blossey, P.: Rain evaporation, snow melt, and entrainment at the heart of water vapor isotopic variations in the tropical troposphere, according to large-eddy simulations and a two-column model, J. Adv. Model. Earth Sci., 13, e2020MS002 381, https://doi.org/10.1029/2020MS002381, 2021.

Risi, C., Muller, C., Vimeux, F., Blossey, P., Védeau, G., Dufaux, C., and Abramian, S.: What controls the mesoscale variations in water isotopic composition within tropical cyclones and squall lines? Cloud resolving model simulations, J. Adv. Model. Earth Sci., 15, e2022MS003 331, https://doi.org/10.1029/2022MS003331, 2023.

Roux, F.: The West African Squall Line Observed on 23 June 1981 during COPT 81: Kinematics and Thermodynamics of the Convective Region, J. Atmos. Sci., 45, 406 – 426, https://doi.org/10.1175/1520-0469(1988)045<0406:TWASLO>2.0.CO;2, 1988.

Roux, F., Testud, J., Payen, M., and Pinty, B.: West African Squall-Line Thermodynamic Structure Retrieved from Dual-Doppler Radar Observations, J. Atmos. Sci., 41, 3104 – 3121, https://doi.org/10.1175/1520-0469(1984)041<3104:WASLTS>2.0.CO;2, 1984.

Seinfeld, J. and Pandis, S.: Atmospheric Chemistry and Physics: From Air Pollution to Climate Change, Wiley, ISBN 9781119221166, 2016.

Smith, J. A., Ackerman, A. S., Jensen, E. J., and Toon, O. B.: Role of deep convection in establishing the isotopic composition of water vapor in the tropical transition layer, Geophys. Res. Lett., 33, https://doi.org/10.1029/2005GL024078, 2006.

Stevens, B., Satoh, M., Auger, L., Biercamp, J., Bretherton, C. S., Chen, X., Düben, P., Judt, F., Khairoutdinov, M., Klocke, D., et al.: DYAMOND: The DYnamics of the atmospheric general circulation modeled on non-hydrostatic domains, Prog. Earth Planet. Sci., 6, 61, https://doi.org/10.1186/s40645-019-0304-z, 2019.

Tanoue, M., Yashiro, H., Takano, Y., Yoshimura, K., Kodama, C., and Satoh, M.: Modeling Water Isotopes Using a Global Non-Hydrostatic Model With an Explicit Convection: Comparison With Gridded Data Sets and Site Observations, J. Geophys. Res. Atmos., 128, e2021JD036 419, https://doi.org/10.1029/2021JD036419, 2023.

Taufour, M., Pinty, J.-P., Barthe, C., Vié, B., and Wang, C.: LIMA (v2.0): A full two-moment cloud microphysical scheme for the mesoscale non-hydrostatic model Meso-NH v5-6, Geosci. Model Dev., 17, 8773–8798, https://doi.org/10.5194/gmd-17-8773-2024, 2024.

Taupin, J.-D. and Gallaire, R.: Variabilité isotopique à l'échelle infra-événement de quelques épisodes pluvieux dans la région de Niamey, Niger, Comptes Rendus de l'Académie des Sciences-Series IIA-Earth and Planetary Science, 326, 493–498, https://doi.org/10.1016/S1251-8050(98)80076-1, 1998.

https://doi.org/10.5194/egusphere-2026-548
Preprint. Discussion started: 9 April 2026

Torri, G., Ma, D., and Kuang, Z.: Stable Water Isotopes and Large-Scale Vertical Motions in the Tropics, J. Geophys. Res. Atmos., 122, 3703–3717, https://doi.org/10.1002/2016JD026154, 2017.

Tremoy, G., Vimeux, F., Soumana, S., Souley, I., Risi, C., Cattani, O., Favreau, G., and Oi, M.: Clustering mesoscale convective systems with laser-based water vapor delta18O monitoring in Niamey (Niger), J. Geophys. Res. Atmos., 119, 5079–5103, https://doi.org/10.1002/2013JD020968, 2014.

Tulet, P., Crassier, V., Solmon, F., Guedalia, D., and Rosset, R.: Description of the Mesoscale Nonhydrostatic Chemistry model and application to a transboundary pollution episode between northern France and southern England, J. Geophys. Res. Atmos., 108, ACH 5–1–ACH 5–11, https://doi.org/10.1029/2000JD000301, 2003.

Tulet, P., Crassier, V., Cousin, F., Suhre, K., and Rosset, R.: ORILAM, a three-moment lognormal aerosol scheme for mesoscale atmospheric model: Online coupling into the Meso-NH-C model and validation on the Escompte campaign, J. Geophys. Res. Atmos., 110, https://doi.org/10.1029/2004JD005716, 2005.

Tulet, P., Grini, A., Griffin, R. J., and Petitcol, S.: ORILAM-SOA: A computationally efficient model for predicting secondary organic aerosols in three-dimensional atmospheric models, J. Geophys. Res. Atmos., 111, https://doi.org/10.1029/2006JD007152, 2006.

Vié, B., Pinty, J.-P., Berthet, S., and Leriche, M.: LIMA (v1.0): A quasi two-moment microphysical scheme driven by a multimodal population of cloud condensation and ice freezing nuclei, Geosci. Model Dev., 9, 567–586, https://doi.org/10.5194/gmd-9-567-2016, 2016.

Vimeux, F., Risi, C., Barthe, C., François, S., Cauquoin, A., Jossou, O., Metzger, J.-M., Cattani, O., Minster, B., and Werner, M.: Is the isotopic composition of precipitation a robust indicator for past reconstructions of tropical cyclones frequency? A case study on Réunion Island from rain and water vapor isotopic observations, J. Geophys. Res. Atmos., 129, e2023JD039 794, https://doi.org/10.1029/2001JD002038, 2024.

Wang, Y. J., Cheng, H., Edwards, R. L., An, Z. S., Wu, J. Y., Shen, C. C., and Dorale, J. A.: A high-resolution absolute-dated late Pleistocene Monsoon record from Hulu Cave, China, Science, 294, 2345–2348, https://doi.org/10.1126/science.1064618, 2001.

Webb, M. J., Lock, A. P., Bretherton, C. S., Bony, S., Cole, J. N., Idelkadi, A., Kang, S. M., Koshiro, T., Kawai, H., Ogura, T., et al.: The impact of parametrized convection on cloud feedback, Phil. Trans. R. Soc. A., 373, https://doi.org/10.1098/rsta.2014.0414, 2015.

Webster, C. R. and Heymsfield, A. J.: Water Isotope Ratios D/H, $^{18}O/^{16}O$, $^{17}O/^{16}O$ in and out of Clouds Map Dehydration Pathways, Science, 302, 1742–1746, https://doi.org/10.1126/science.1089496, 2003.

Wing, A. A., Reed, K. A., Satoh, M., Stevens, B., Bony, S., and Ohno, T.: Radiative-Convective Equilibrium Model Intercomparison Project, Geosci. Model Dev., 11, 793–813, https://doi.org/10.5194/gmd-11-793-2018, 2018.

Worden, J., Noone, D., and Bowman, K.: Importance of rain evaporation and continental convection in the tropical water cycle, Nature, 445, 528–532, https://doi.org/10.1038/nature05508, 2007.

https://doi.org/10.5194/egusphere-2026-548
Preprint. Discussion started: 9 April 2026

Table 1. Set of parameters used to characterize each hydrometeor category in the ICE3 microphysics scheme

Parameters	Cloud droplets	Raindrops	Pristine ice	Snow/aggregates	Graupel
α	3 on sea; 1 on land	1	3	1	1
ν	1 on sea; 3 on land	1	3	1	1
a	524	524	0.82	0.02	19.6
b	3	3	2.5	1.9	2.8
c	$3.2\ 10^7$	842	800	5.1	124
d	2	0.8	1	0.27	0.66
C	-	$8\ 10^6$	-	5	$5\ 10^5$
x	-	-1	-	1	-0.5
f_0	-	1	1	0.86	0.86
f_1	-	0.26	-	0.28	0.28
f_2	-	-	0.14	-	-
$\mathcal{C}_1$	-	0.5	$1/\pi$	$1/\pi$	0.5

https://doi.org/10.5194/egusphere-2026-548
Preprint. Discussion started: 9 April 2026

Table 2. List of symbols

Symbols	Description	SI units
a	Parameter for the mass-diameter relationship	$\mathrm{kg\,m^{-b}}$
A	Factor in the expression of $\Delta r_c^{\mathrm{iso}}\big\vert_{\mathrm{CND/EVA}}$	-
A_i	Thermodynamical function for diffusional growth of ice particles	
A_w	Thermodynamical function for raindrop evaporation	
b	Parameter for the mass-diameter relationship	-
c	Parameter for the fall-speed-diameter relationship	$\mathrm{m^{1-d}\,s^{-1}}$
c'	Factor in the expression of $\Delta r_r\vert_{\mathrm{EVA}}$	
c'^{iso}	Factor in the expression of $\Delta r_r^{\mathrm{iso}}\big\vert_{\mathrm{EVA}}$	
C	Parameter for the $N = C\lambda^x$ relationship	
$\mathcal{C}_1$	Parameter for the relationship ($\mathcal{C} = \mathcal{C}_1 D$)	-
d-excess	Deuterium excess	
d	Parameter for the fall-speed-diameter relationship	-
D	Hydrometeor diameter	m
$\mathcal{D}_v$	Molecular diffusivity of light water vapor in air	$\mathrm{m^2\,s^{-1}}$
$\mathcal{D}_v^{\mathrm{iso}}$	Molecular diffusivity of heavy water vapor in air	
$e_{\mathrm{si}}(T)$	Saturation vapor pressure over ice	Pa
$e_{\mathrm{sw}}(T)$	Saturation vapor pressure over liquid water	Pa
f	Ventilation factor for light particles	-
f^{iso}	Ventilation factor for heavy particles	-
f_0, f_1, f_2	Parameters to compute the ventilation factor	-
F	Factor in the expression of α_K	
$g(D)$	Generalized gamma distribution law	-
k_a	Thermal conductivity of air	$\mathrm{kg\,m\,s^{-3}\,K^{-1}}$
L_s	Latent heat of sublimation	$\mathrm{J\,kg^{-1}}$
L_v	Latent heat of vaporization	$\mathrm{J\,kg^{-1}}$
m	Hydrometeor mass	kg
m_r	Mass of a raindrop	kg
m_r^{iso}	Mass of a raindrop containing heavy isotopes	kg
$M(p)$	p-order moment of the particle size distribution	-
$n(D)$	Number conc. of hydrometeors with $D <$ diameter $< D + dD$	$\mathrm{kg^{-1}\,m^{-1}}$
N	Number concentration of hydrometeors	$\mathrm{kg^{-1}}$
N_c	Number concentration of cloud droplets	$\mathrm{kg^{-1}}$
N_r	Number concentration of raindrops	$\mathrm{kg^{-1}}$

https://doi.org/10.5194/egusphere-2026-548
Preprint. Discussion started: 9 April 2026

Table 3. List of symbols

Symbols	Description	SI units
N_{Re}	Reynolds number	-
$N_{\mathrm{Sc,v}}$	Schmidt number for water vapor	-
$N_{\mathrm{Sc,v}}^{\mathrm{iso}}$	Schmidt number for heavy molecules of water vapor	-
p	Pressure	Pa
p_0	Standard atmospheric pressure at the ground level	Pa
r	Mixing ratio	$\mathrm{kg\,kg^{-1}}$
r^{iso}	Isotopic mixing ratio for $H_2^{18}O$ and HDO	$\mathrm{kg\,kg}-1$
r_c	Cloud droplet mixing ratio	$\mathrm{kg\,kg^{-1}}$
r_c^{iso}	Heavy mixing ratio of cloud droplets	$\mathrm{kg\,kg^{-1}}$
r_r	Raindrop mixing ratio	$\mathrm{kg\,kg^{-1}}$
r_r^{iso}	Heavy mixing ratio of raindrops	$\mathrm{kg\,kg^{-1}}$
r_v	Water vapor mixing ratio	$\mathrm{kg\,kg^{-1}}$
r_v^{iso}	Heavy mixing ratio of water vapor	$\mathrm{kg\,kg^{-1}}$
R	Isotope ratio	-
R_c	Isotope ratio in cloud water	-
R_i	Isotope ratio in ice	-
R_l	Isotope ratio in liquid condensate	-
R_w	Isotope ratio in water vapor	-
R_{VSMOW}	Isotope ratio in the Vienna Standard Mean Ocean Water	-
$\mathcal{R}_v$	Specific gas constant for water vapor	$\mathrm{J\,kg^{-1}\,K^{-1}}$
S^{iso}	Source term for heavy water variables	
S_i	Supersaturation over ice	-
S_l	Supersaturation over liquid water	-
T	Temperature	K
T_0	Standard atmospheric temperature	K
$\mathbf{U}$	3D air velocity	$\mathrm{m\,s^{-1}}$
v	Hydrometeor terminal fall speed	$\mathrm{m\,s^{-1}}$
x	Parameter for the $N = C\lambda^x$ relationship	-
α	Parameter for the hydrometeors size distributions	-
α_K	Kinetic fractionation coefficient	-
$\alpha_{i/v}$	Equilibrium fractionation factor between ice and water vapor	
$\alpha_{l/v}$	Equilibrium fractionation factor between liquid and water vapor	
δ	Isotopic composition	‰
$\delta^{18}\mathrm{O}$	Isotopic composition in $H_2^{18}O$	‰
$\delta^{18}\mathrm{O}_e$	$\delta^{18}O$ in the evaporation flux	‰

https://doi.org/10.5194/egusphere-2026-548
Preprint. Discussion started: 9 April 2026

Table 4. List of symbols

Symbols	Description	SI units
$\delta^{18}O_p$	δ^{18}O of rain	‰
$(\delta^{18}O_p)_{eq}$	δ^{18}O of rain in equilibrium with water vapor	‰
$\delta^{18}O_v$	δ^{18}O of water vapor	‰
δD	Isotopic composition in HDO	‰
$\Delta r\|_{\text{ACC}}$	Mass mixing ratio transfer rate during accretion of cloud droplets by snow	$\mathrm{kg\,kg^{-1}\,s^{-1}}$
$\Delta r^{\text{iso}}\|_{\text{ACC}}$	Mass mixing ratio transfer rate during accretion of cloud droplets by snow for heavy isotopes	$\mathrm{kg\,kg^{-1}\,s^{-1}}$
$\Delta r\|_{\text{DEP}}$	Mass mixing ratio transfer rate during deposition of water vapor on ice particles	$\mathrm{kg\,kg^{-1}\,s^{-1}}$
$\Delta r^{\text{iso}}\|_{\text{DEP}}$	Mass mixing ratio transfer rate during deposition of water vapor on ice particles for heavy isotopes	$\mathrm{kg\,kg^{-1}\,s^{-1}}$
$\Delta r\|_{\text{SUB}}$	Mass mixing ratio transfer rate during sublimation of ice particles	$\mathrm{kg\,kg^{-1}\,s^{-1}}$
$\Delta r^{\text{iso}}\|_{\text{SUB}}$	Mass mixing ratio transfer rate during sublimation of ice particles for heavy isotopes	$\mathrm{kg\,kg^{-1}\,s^{-1}}$
$\Delta r\|_{\text{CND/EVA}}$	Mass mixing ratio transfer rate during condensation / evaporation of cloud droplets	$\mathrm{kg\,kg^{-1}\,s^{-1}}$
$\Delta r^{\text{iso}}\|_{\text{CND/EVA}}$	Mass mixing ratio transfer rate during condensation / evaporation of cloud droplets for heavy isotopes	$\mathrm{kg\,kg^{-1}\,s^{-1}}$
$\Delta r_r\|_{\text{EVA}}$	Mass mixing ratio transfer rate during raindrop evaporation	$\mathrm{kg\,kg^{-1}\,s^{-1}}$
$\Delta r_r^{\text{iso}}\|_{\text{EVA}}$	Mass mixing ratio transfer rate during raindrop evaporation for heavy isotopes	$\mathrm{kg\,kg^{-1}\,s^{-1}}$
$\eta(T)$	Dynamic viscosity of air	$\mathrm{Pa\,s}$
χ	Variable in the expression of the ventilation coefficient for light water	-
χ_{iso}	Variable in the expression of the ventilation coefficient for heavy water	-
$\Gamma()$	Gamma function	-
λ	Slope parameter of the hydrometeors size distribution	$\mathrm{m^{-1}}$
ν	Parameter for the hydrometeors size distributions	-
$\nu(T)$	Dynamic viscosity of air	$\mathrm{Pa\,s}$
ρ_0	Air density at the reference pressure level	$\mathrm{kg\,m^{-3}}$
ρ_a	Dry air density	$\mathrm{kg\,m^{-3}}$
ρ_w^{iso}	Density of heavy water vapor for the environment	$\mathrm{kg\,m^{-3}}$
$\rho_{w,D}^{\text{iso}}$	Density of heavy water vapor on the surface of the raindrop	$\mathrm{kg\,m^{-3}}$